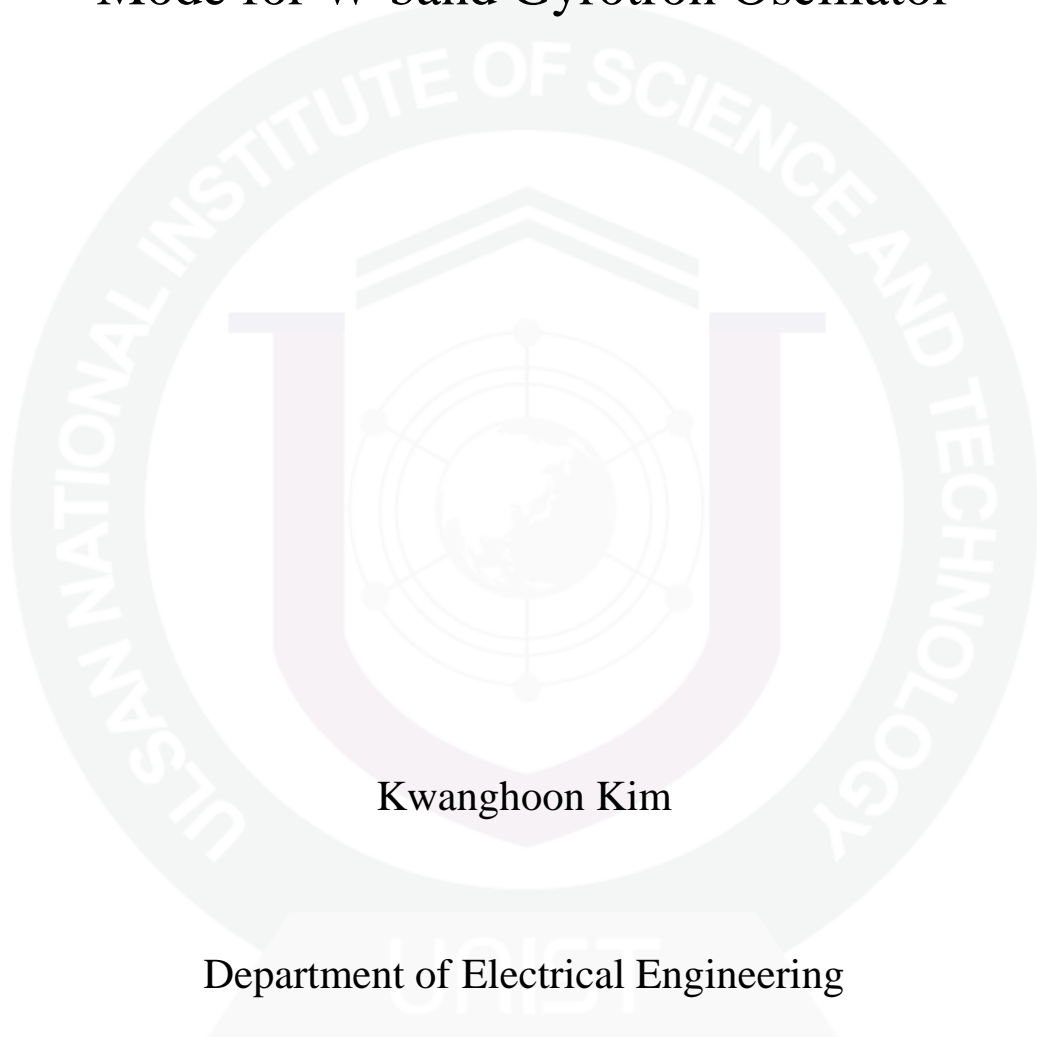


Experimental Study on Generation of a Higher Order
Mode for W-band Gyrotron Oscillator



Kwanghoon Kim

Department of Electrical Engineering

Graduate school of UNIST

2013

Experimental Study on Generation of a Higher Order Mode for W-band Gyrotron Oscillator

Kwanghoon Kim

Department of Electrical Engineering

Graduate school of UNIST

Experimental Study on Generation of a Higher Order Mode for W-band Gyrotron Oscillator

A thesis

Submitted to the Graduate School of UNIST

In partial fulfillment of the requirement for the degree of

Master of Science

Kwanghoon Kim

06.26.2013

Approved by



Major Advisor

EunMi Choi

Experimental Study on Generation of a Higher Order Mode for W-band Gyrotron Oscillator

Kwanghoon Kim

This certifies that thesis of Kwanghoon Kim is approved

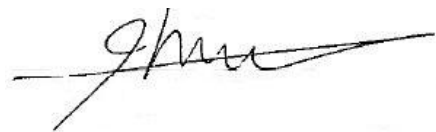
06.26.2013 of submission

Signature



Thesis Supervisor: EunMi Choi

Signature



Typed name: MinSup Hur

Signature



Typed name: MinSuk Kwon

Abstract

This thesis reports the design and experimental demonstration of a mode generator for a TE_{62} mode, operating at 95 GHz. The excitation of a target mode for a cold test has been performed in the mode generator. The cavity mode of a mode generator excites the TE_{62} mode by means of a fundamental mode. A TE_{62} mode was chosen as a cavity mode for a W-band Gyrotron. In order to test the performance, the TE_{62} mode generator has been developed for a cold test.

Quasi-optical analysis has been done for designing mode generator. A Gaussian-like beam from a corrugated feed horn using a vector network analyzer propagates to the cavity which was made translucent by array of holes. The measurement is very sensitive to the experimental conditions such as coupling of the cavity, alignment, and undesirable interception from the reflected beam. Simulations were done by High Frequency Structure Simulator (HFSS) and CST MICROWAVE STUDIO (CST MWS), and then compared to the experimental results.

Contents

I.	Introduction	14
	1.1 Motivation of this research.....	15
	1.2 Mode generator	16
	1.3 Gaussian beam	16
II.	Theory of mode generator	18
	2.1 Corrugated feed horn.....	18
	2.1.1 Hybrid modes.....	18
	2.1.2 Gaussian-like beam of a corrugated waveguide.....	19
	2.1.3 Gaussian modes	19
	2.2 Mirror system.....	20
	2.2.1 Parabolic Mirror.....	20
	2.2.2 Elliptic mirror	21
	2.3 Cavity	23
	2.3.1 Electromagnetic fields of a cavity	23
III.	Design and experiment of a mode generator	25
	3.1 Design and experiment of a corrugated feed horn	25
	3.2 Design and experiment of a mirror	32
	3.3 Design and experiment of a cavity	40
	3.3.1 Comparison between counter clockwise and clockwise	48
	3.3.2 Inserting an inner rod in a cavity.....	50
	3.3.3 Changing the measurement distance.....	52
	3.3.4 Two mirror system of a mode generator	55

IV. Summary & Conclusion67

List of Figures

Figure 1-1. Mode generator consists of horn, mirror, and coaxial cavity.

Figure 1-2. Mode conversion from Gaussian to TE_{62} mode.

Figure 1-3. The characteristic of Gaussian beam

Figure 2-1. Parabolic mirror (A) Geometry (B) reflected beam of off axis paraboloid

Figure 2-2. Geometry of ellipsoidal mirror.

Figure 3-1. Schematic of a corrugated waveguide

Figure 3-2. Corrugated feed horn (WR-08)

Figure 3-3. 95GHz corrugated horn

Figure 3-4. The structure of 95GHz corrugated horn.

Figure 3-5. Simulation results of the corrugated feed horn (E field pattern).

Figure 3-6. Experimental environment for the horn.

Figure 3-7. Experimental results of 0mm distance from a horn aperture to open-cut waveguide (A) Amplitude plot by 12dB (B) 3D amplitude plot (C) 1D amplitude plot (D) 1D phase plot

Figure 3-8. Experimental results of 50mm distance from a horn aperture to open-cut waveguide. (A) Amplitude plot by 12dB (B) 3D amplitude plot (C) 1D amplitude plot (D) 1D phase plot

Figure 3-9. Experimental results of 100mm distance from a horn aperture to open-cut waveguide. (A) Amplitude plot by 12dB (B) 3D amplitude plot (C) 1D amplitude plot (D) 1D phase plot

Figure 3-10. Data comparison plots of measurement, calculation and simulation results. It is propagated from corrugated feed horn.

Figure 3-11. The design drawing of a parabolic mirror

Figure 3-12. Simulation results on E-field pattern at mirror.

Figure 3-13. 1D amplitude plot of mirror simulation from reflected mirror

Figure 3-14. Experimental environment of reflected beam from mirror

Figure 3-15. Experimental results of 15mm distance from reflected mirror to open-cut waveguide. (A) 2D amplitude plot (B) Amplitude plot by 12dB (C) 1D amplitude plot of x axis (D) 1D amplitude plot of y axis (E) 1D phase plot

Figure 3-16. Experimental results of 20mm distance from reflected mirror to open-cut waveguide. (A) 2D amplitude plot (B) Amplitude plot by 12dB (C) 1D amplitude plot of x axis (D) 1D amplitude plot of y axis (E) 1D phase plot

Figure 3-17. Experimental results of 15mm distance from reflected mirror to open-cut waveguide. (A) 2D amplitude plot (B) Amplitude plot by 12dB (C) 1D amplitude plot of x axis (D) 1D amplitude plot of y axis (E) 1D phase plot

Figure 3-18. Data comparison plots of measurement, calculation and simulation results. It is propagated from reflected mirror

Figure 3-19. Geometrical optics view of a cylindrical waveguide

Figure 3-20. Schematic of coaxial cavity

Figure 3-21. Schematic of holes on coaxial cavity wall. The section consists of 15 axially \times 25 azimuthally

Figure 3-22. The picture of the coaxial cavity. Due to good coupling, the cavity thickness changed from 2mm to 0.2mm

Figure 3-23. CASCADE Code Simulation. (a) CASCADE View (b) S21 Amplitude TE_{62} mode

Figure 3-24. Simulation set-up for a hole structure cavity using HFSS program (a) Excitation view (b)

Mesh set-up: 0.6667 Lambda

Figure 3-25. Coupling simulation of a cavity using HFSS program (E-field pattern).

Figure 3-26. Simulation results of CST for pattern of each axis. (A) x-axis E-field pattern (B) y-axis E-field pattern (C) Sum E-field pattern

Figure 3-27. Experimental environment of a mode generator. (A) Experiment using scan device (B) A mode generator

Figure 3-28. Propagating to cavity. (A) The counter clockwise (B) The clockwise

Figure 3-29. E-field Magnitude pattern of the counter clockwise. (A) The vertical axis (B) The horizontal axis (C) The sum of vertical and horizontal axis

Figure 3-30. E-field Magnitude pattern of the clockwise and insertion of the inner rod. (A) The vertical axis (B) The horizontal axis (C) The sum of vertical and horizontal axis

Figure 3-31. E-field Magnitude pattern of no insertion of the inner rod in the cavity. (A) The vertical axis (B) The horizontal axis (C) The sum of vertical and horizontal axis

Figure 3-32. Modification of measurement environment such as absorber and arrangement

Figure 3-33. 1mm distance measurement from aperture to open waveguide probe, the vertical E-field magnitude pattern

Figure 3-34. 1mm distance measurement from aperture to open waveguide probe, the horizontal E-field magnitude pattern

Figure 3-35. 1mm distance measurement from aperture to open waveguide probe, The sum of vertical and horizontal axis magnitude

Figure 3-36. The most optimized 1D amplitude plot through rotating axis of measurement data

Figure 3-37. Curvature of a geometrical optics

Figure 3-38. Schematic of the two mirror system

Figure 3-39. M1 measurement results for the vertical axis (by 12dB)

Figure 3-40. Comparison with ideally Gaussian beam and M1 measurement results for the vertical axis

Figure 3-41. M1 measurement results for the horizontal axis

Figure 3-42. Comparison with ideally Gaussian beam and M1 measurement results for the horizontal axis

Figure 3-43. M2 measurement results (by 12dB)

Figure 3-44. Comparison with ideally Gaussian beam and M2 measurement results for the vertical axis

Figure 3-45. Comparison with ideally Gaussian beam and M2 measurement results for the horizontal axis

Figure 3-46. The measurement environment of two mirror system

Figure 3-47. 1mm distance measurement from aperture to open waveguide probe, the vertical E-field magnitude pattern (Two mirror system).

Figure 3-48. 1mm distance measurement from aperture to open waveguide probe, the horizontal E-field magnitude pattern (Two mirror system).

Figure 3-49. 1mm distance measurement from aperture to open waveguide probe. The dB sum of vertical and horizontal axis (Two mirror system).

Figure 3-50. The measurement environment of G.A mode generator.

Figure 3-51. 1mm distance measurement from aperture of G.A generator to open waveguide probe. The dB sum of vertical and horizontal axis.

Figure 3-52. 10mm distance measurement from aperture of G.A generator to open waveguide probe. The dB sum of vertical and horizontal axis.

Figure 3-53. The most optimized 1D amplitude at radial axis plot through rotating axis of measurement data. Measurement result of UNIST mode generator was compared with G.A generator data.

Figure 3-54. The most optimized 2D amplitude at azimuthal axis plot through rotating axis of measurement data. Measurement result of UNIST mode generator was compared with G.A generator data.

List of Tables

Table 2-1. $HE_{1,1}$ mode decomposition in terms of $TE_{1,n}$ and $TM_{1,n}$ modes.

Table 3-1. Computer resources of corrugated feed horn simulation.

Table 3-2. The parameter setting for horn simulation

Table 3-3. Data comparison of measurement, calculation and simulation text results. It is propagated from corrugated feed horn

Table 3-4. The parameter setting for horn simulation

Table 3-5. Design parameter of the cavity

Table 3-6. Simulation results of CASCADE Code (Input mode: TE_{62} mode).

Table 3-7. Simulation set-up of hole structure cavity using waveguide port.

Table 3-8. Computer specification for simulation of coupling

Chapter 1

Introduction

A mode generator that is part of the gyrotron mainly studied by Germany, Russia, and USA. The low power excitation using quasi-optical techniques was studied by N. L. Alexandrov in Russia (1995) [1]. The experimental results of low power excitation of a 118GHz at $TE_{22.6}$ mode are presented. Fundamental modes of rectangular waveguide are converted to a $TE_{22.6}$ mode using quasi-optical techniques. The converter using a coaxial cavity was designed and tested. The design methods for the quasi-optical system are shown that convert the input Gaussian beam to a desired beam which will excite the $TE_{22.6}$ mode in the given coaxial cavity. This paper shown the converter is presently being successfully used to perform low power verification of the quasi-optical system design for a 118GHz at $TE_{22.6}$ gyrotron. And the mode generator was studied by D. Wagner in Germany (2002) [2]. This paper studied several high order cavity modes have to be excited at low power levels. Because they want to verify the performance of broadband quasi-optical mode converters of gyrotrons in cold-test experiments. The frequency range to be covered is 105-140 GHz. The preferred method is the direct excitation of a cavity through a translucent cavity wall. They studied mode generator consisting of dual-mode horn, two cylindrical lenses, and a quasi-parabolic mirror. This paper shown good agreement with the calculated and measured mode pattern of the $TE_{22.8}$ mode at 140 GHz. A mode generator has positive effect of the wide area such as military field, medical field, and bio-technology, therefore, we started this research.

The mode generator typically excites a target mode for a cold test by exciting a cavity mode. A TE_{62} mode was chosen to beam cavity mode for W-band Gyrotron [3]. In order to test the performance of the Gyrotron cavity, the TE_{62} mode generator has been developed for a cold test [2]. The mode generator usually consists of a corrugated feed horn, mirrors and a resonator. The basic set-up of the mode generator is shown in Figure 1-1 [1].

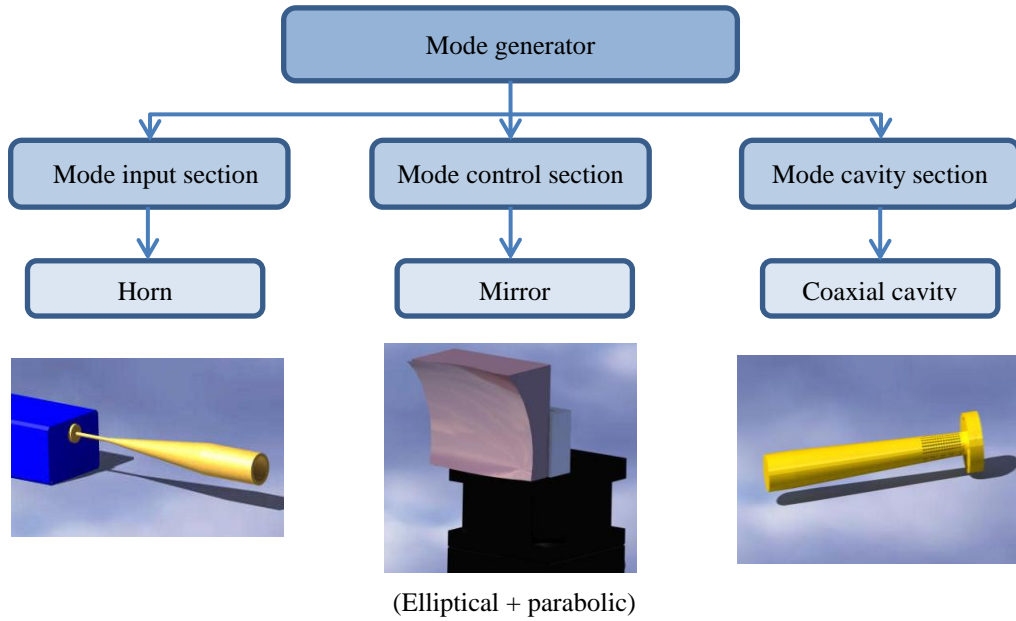


Figure 1-1: Mode generator consists of horn, mirror, and coaxial cavity.

A generated Gaussian beam from a horn antenna propagates to mirror system [4]. The mirrors are either parabolic shape or elliptical shape in perpendicular and parallel direction with respect to the beam propagation direction. Each directional component has been analyzed separately to determine the Gaussian beam size as the beam propagates using quasi-optical theory. Gaussian beam is focused at caustic through a translucent cavity wall. As shown in Figure 1-2, mode generation system is converted from Gaussian beam to TE_{62} mode.

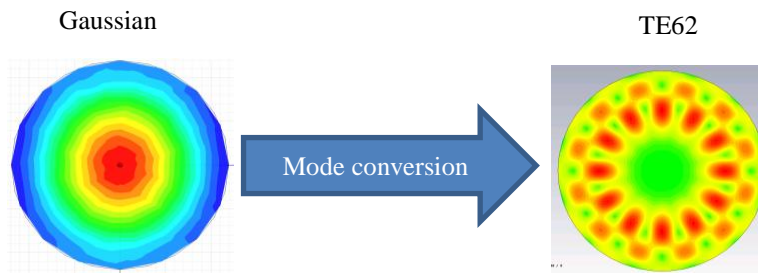


Figure 1-2: Mode conversion from Gaussian to TE_{62} mode.

1.1 Mode generator

The motivation of the research is the development of a generation of higher order mode for W-band gyrotron oscillator. The mode generator is needed for cold test of a mode converter system of a high power gyrotron. After generating low mode at input part, we have to control beam by adjusting the size and position of beam using mirrors [5]. The cavity excites the target mode by coupling the beam

reflected off mirror arrays. As a result, the cavity at the aperture generates the desired higher-order modes [6].

1.2 gyrotorn

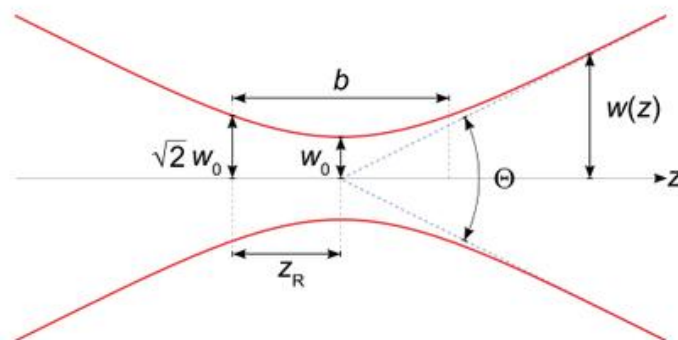
A gyrotron is a vacuum electronic device (VED) to generate high power and high frequency radiation. The operation of a gyrotron is based on the stimulated cyclotron radiation which is electron oscillation in a strong magnetic field [7].

The electron emitted from the Electron gun in the gyrotron will come out through the cavity and the mode convertor [8]. A cavity in the gyrotron excites the desired mode by coupling from the electron beam [9]. The mode convertor is converted from selected mode to a gaussian beam.

1.3 Gaussian beam

In order to apply to low power of the cavity at the input part, Gaussian mode is appropriate for designing quasi-optical mirror system. Gaussian beam with high transmission efficiency characteristics of the distribution of the electric field and magnetic field antennas are used [10].

What is Gaussian beam? Figure 1-3 shows the characteristics of a Gaussian beam [11]. When beam goes to the focus, it is the smaller beam width at the focus ($z=0$). The size of the beam passed through a focus linearly expands again.



Picture 1-3: The characteristic of Gaussian beam [12]

In order to derive the Gaussian beam formula, we assume that the electromagnetic wave progress the $+z$ direction. In addition, Gaussian beam changed to propagate z direction such as Gaussian function [13].

$$E(\vec{r}) = A(z) \exp \left[i \frac{k\rho^2}{2q(z)} \right] \cdot e^{ikz}, \text{ where } \rho^2 = x^2 + y^2 \quad (1.1)$$

Where k is a wave number. When Gaussian beam propagates to z axis, a few condition changed such as beam width and phase. According to these, one may consider that $q(z)$ is complex number.

$$q(z) = z - iz_R \quad (1.2)$$

$$\frac{1}{q(z)} = \frac{z}{z^2 + z_R^2} + i \frac{z_R}{z^2 + z_R^2} = \frac{1}{R(z)} + i \frac{2}{kW^2(z)} \quad (1.3)$$

z_R is not determined by equation 1.2. To arrange z_R , we can consider figure 1-3.

$$z = 0, w_0 = w(0) \quad (1.4)$$

$$\frac{1}{z_R} = \frac{2}{kW_0^2}, \quad z_R = \frac{kW_0^2}{2} = \frac{\pi W_0^2}{\lambda} \quad (1.5)$$

$$w(z) = w_0 \sqrt{1 + \frac{z^2}{z_R^2}} \quad (1.6)$$

The beam waist (w_0) is the smaller beam width by reference figure 1.3. So it can be measured. z_R is determined by equation 3. z_R is called as the Rayleigh length or the Rayleigh range [12]. $w(z)$ is increased to sqrt 2 times at $z = z_R$. The position of $z = z_R$ is the Rayleigh length. The beam radius is distance to the position of the maximum intensity $1/e^2$ (13.5%).

$$z_R = \frac{\pi W_0^2}{\lambda} \quad (1.7)$$

When linearly increasing the beam, we can know angle (θ is radians) [14].

$$\theta \simeq \frac{\lambda}{\pi W_0} \quad (1.8)$$

The cavity transforms the Gaussian-like beam into a TE mode, which is guided to a cavity aperture.

Chapter 2

Theory of Mode Generator

2.1 Corrugated Feed Horn

2.1.1 Hybrid modes

The TM and TE modes which are direct equation of the wave equation inside a smooth circular waveguide are fundamental modes in a circular waveguide. But if the waveguide is corrugated, it could be also useful to define the field inside the smooth circular waveguide by the hybrid modes EH and HE. So in fact we can choose to define the field inside the corrugated horn antenna is term of TE and TM modes or in terms of HE and EH modes [15].

Transvers electric and magnetic modes are well known in waveguide theory. A simple physical description of the properties of hybrid modes is going to be discussed.

If we assume hybrid condition, it can be defined with the following simplified equation [16]

HE_{m,n} modes

$$E_x(r, \phi) = \frac{\sqrt{2 \cdot Z_0}}{R \cdot \sqrt{\pi}} \cdot \frac{J_{m-1}\left(\frac{\chi_{m,n} \cdot r}{R}\right)}{J'_{m-1}(\chi_{m,n})} \cdot \cos[(m-1) \cdot \phi] \quad (2.1)$$

$$E_y(r, \phi) = \frac{\sqrt{2 \cdot Z_0}}{R \cdot \sqrt{\pi}} \cdot \frac{J_{m-1}\left(\frac{\chi_{m,n} \cdot r}{R}\right)}{J'_{m-1}(\chi_{m,n})} \cdot \sin[(m-1) \cdot \phi] \quad (2.2)$$

EH_{m,n} modes

$$E_x(r, \phi) = \frac{\sqrt{2 \cdot Z_0}}{R \cdot \sqrt{\pi}} \cdot \frac{J_{m+1}\left(\frac{\chi_{m,n} \cdot r}{R}\right)}{J'_{m-1}(\chi_{m,n})} \cdot \cos[(m+1) \cdot \phi] \quad (2.3)$$

$$E_y(r, \phi) = \frac{\sqrt{2 \cdot Z_0}}{R \cdot \sqrt{\pi}} \cdot \frac{J_{m+1}\left(\frac{\chi_{m,n} \cdot r}{R}\right)}{J'_{m-1}(\chi_{m,n})} \cdot \sin[(m+1) \cdot \phi] \quad (2.4)$$

Where $\chi_{m,n}$ are the roots of the Bessel functions ($J_{m-1}(x) = 0$ for the HE modes and $J_{m+1}(x) = 0$ for EH modes), R is the waveguide radius, m and n the radial and azimuthal indexes of the modes and Z_0 is the impedance of free space.

2.1.2 Gaussian-like beam of a corrugated waveguide

The $HE_{1,1}$ mode is the fundamental mode of a corrugated waveguide at the aperture [17]. From Eq. (2.1), this mode is defined only by a distinct component

$$E_x(r, \varnothing) = \frac{\sqrt{2 \cdot Z_0}}{R \cdot \sqrt{\pi}} \cdot \frac{J_0\left(\frac{\chi_{1,1} \cdot r}{R}\right)}{J'_0(\chi_{1,1})}$$

$$E_y(r, \varnothing) = 0 \quad (2.5)$$

where $\chi_{1,1}$ is the root of the Bessel function $J_0(x) = 0$ and in this particular case, for the $HE_{1,1}$ mode is $\chi_{1,1}=2.404$. Equation 2.5 can be obtained from a particularization of Eq. (2.1) and (2.2).

TE modes	TM modes
$TE_{1,1}$ 84.496 %	$TM_{1,1}$ 14.606 %
$TE_{1,2}$ 0.082 %	$TM_{1,2}$ 0.613%
$TE_{1,3}$ $3.58 \cdot 10^{-3}\%$	$TM_{1,3}$ 0.121%
$TE_{1,4}$ $4.94 \cdot 10^{-4}\%$	$TM_{1,4}$ 0.039%

Table 2-1: $HE_{1,1}$ mode decomposition in terms of $TE_{1,n}$ and $TM_{1,n}$ modes

The $HE_{1,1}$ mode can be described as a combination of TM and TE modes. The $HE_{1,1}$ mode is approximately a combination of 15 % ($TM_{1,1}$) and 85 % ($TE_{1,1}$) with the adequate phase shift them. But in fact, this mode mixture is not perfect, (99.2 % efficient with $HE_{1,1}$ mode), the perfect mode mixture in terms of smooth waveguide modes, supposing hybrid condition can be seen in table 2-1 [18, 19].

2.1.3 Gaussian modes

It is well known that one of the best ways to define a free space radiation from an antenna is by beams of the paraxial free space modes, the Gaussian modes, which are a solution of the paraxial free space equation [20].

$$E(r, \varphi, z) = \frac{W_0}{W(z)} \cdot e^{\frac{-r^2}{w^2(z)}} \cdot e^{-\frac{kr^2}{2 \cdot R(z)}} \cdot e^{-j(kz - \zeta(z))} \quad (2.6)$$

where $r^2 = x^2 + y^2$ and $w(z)$ is the beamwidth where there is a field decay of 1/e respect to the maximum. In $z=0$, the function $w(z)$ in Eq. (2.7), has a minimum known as beamwaist and called w_0 .

$$W(z) = W_0 \cdot \sqrt{1 + \left(\frac{z}{k \cdot w_0}\right)^2} \quad (2.7)$$

It is important also to check the similarity between the fundamental Gaussian mode and the $HE_{1,1}$ mode at a certain diameter aperture.

2.2 Mirror system

2.2.1 Parabolic Mirror

The paraboloid is formed by rotating a parabola about the axis including its vertex and its focus that is taken to be the z axis as indicated in Figure 2-1. The resulting surface having its vertex at the origin is described by

$$z = \frac{x^2 + y^2}{4 f_p} \quad (2.8)$$

Where f_p denoted the focal length. It is generally more convenient to use a spherical polar coordinate system with origin at the focal point, in which the surface is described by

$$\rho = \frac{2 f_p}{1 + \cos \theta} \quad (2.9)$$

As shown in Figure 2-1, ρ is the distance from the origin to a point P on the surface and θ is the angle between the axis of symmetry and the line between the focus and point P. The polar angle θ about the z axis varies between 0 and 2π , but in much of what follows we will consider only the parabolic curve defined for $\theta = 0$, which thus lies in the x, z plane [21, 22].

An incident ray parallel to the z axis in the x, z plane makes an angle θ_i , relative to the local normal to the reflective surface.

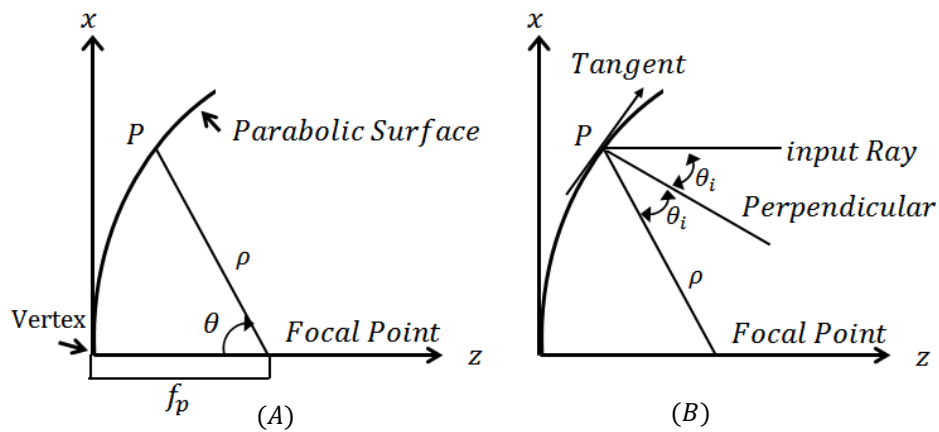


Figure 2-1 Parabolic mirror (A) Geometry (B) reflected beam of off axis paraboloid.

2.2.2 Elliptical Mirror

Ellipsoid takes rotationally symmetric about its major axis, which as shown in figure 3 is the z axis. The major axis has length $2a$, and the mirror axis perpendicular to this has length $2b$. The equation of the ellipsoid surface in Cartesian coordinates is [23]

$$\frac{x^2+y^2}{b^2} + \frac{z^2}{a^2} = 1 \quad (2.10)$$

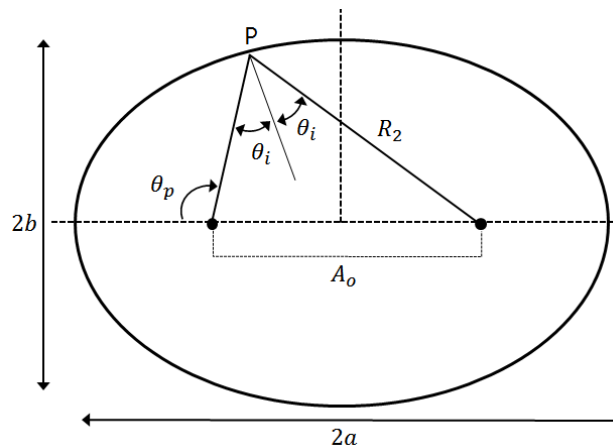


Figure 2-2 Geometry of ellipsoidal mirror.

And the distances from the two focal points F_1 and F_2 , denoted R_1 and R_2 , respectively, to a point p on the surface are related by

$$R_1 + R_2 = 2a \quad (2.11)$$

The separation of the point is

$$A_0 = 2ea \quad (2.12)$$

Focusing elements are used as shown in Figure 3. We define θ_i to be the angle of incidence of the beam relative to the local surface normal and consider an ellipse used to bend the beam in the x, z plane.

2.3 Cavity

The cavity of a gyrotron oscillator considered here takes the type of a cylindrical waveguide of radius r_{cavity} . Modes propagated by an electron beam have the transverse pattern of a TE mode with an axial field along the cavity axis z.

2.3.1 Electromagnetic Fields of a cavity [24]

In a free-air medium without electric charge density and current sources ($\rho = 0, J = 0$) and with related equations $B = \mu_0 H$, and $D = \epsilon_0 E$, Maxwell's equation can be written as below at a frequency ω .

$$\nabla \times E = -j\omega\mu_0 H \quad (2.13)$$

$$\nabla \times H = j\omega\epsilon_0 E \quad (2.14)$$

$$\nabla \cdot E = 0 \quad (2.15)$$

$$\nabla \cdot H = 0 \quad (2.16)$$

Where H represents the magnetic field density, B represents the magnetic flux density, E represents the electric field density, D represents the electric displacement, $\epsilon_0 = 8.854187817 \times 10^{-12}$ farad/m is the permittivity of free space, and $\mu_0 = 4\pi \times 10^{-7}$ henry/m is the permeability of free space. Follow equation 2.15 and 2.16, E and H can be expressed as functions of the magnetic vector potential A and electric vector potential

$$H = \nabla \times A \quad (2.17)$$

$$E = -\nabla \times F \quad (2.18)$$

Solvable Eq. (2.14) and (2.18), the magnetic field H is

$$\mathbf{H} = -j\omega\epsilon_0\mathbf{F} + \nabla\varphi \quad (2.19)$$

with φ denoting an arbitrary scalar function. We can obtain the wave equation for the electric vector potential F

$$(\nabla^2 + \omega^2\mu_0\epsilon_0)\mathbf{F} = 0 \quad (2.20)$$

For TE case in cylindrical coordinates (ρ, ϕ, z) and considering $\mathbf{F} = \psi\hat{z}$, the E and H are

$$\mathbf{E} = -\frac{1}{\rho}\frac{\partial\psi}{\partial\phi}\hat{\rho} + \frac{\partial\psi}{\partial\rho}\hat{\phi} \quad (2.21)$$

$$\mathbf{H} = -\frac{j}{\omega\mu_0}\frac{\partial^2\psi}{\partial\rho\partial z}\hat{\rho} - \frac{j}{\omega\mu_0\rho}\frac{\partial^2\psi}{\partial\phi\partial z}\hat{\phi} - \frac{j}{\omega\mu_0}\left(\omega^2\mu_0\epsilon_0\psi + \frac{\partial^2\psi}{\partial z^2}\right)\hat{z} \quad (2.22)$$

Where the function ψ can be found as a solution of the wave equation $(\nabla^2 + \omega^2\mu_0\epsilon_0)\psi = 0$ using separation of variables $\psi(\rho, \phi, z) = AR(\rho)\Phi(\phi)Z(z)$ where A is a constant [25]

$$\frac{1}{\rho R}\frac{\partial}{\partial\rho}\left(\rho\frac{\partial R}{\partial\rho}\right) + \frac{1}{\rho^2\Phi}\frac{\partial^2\Phi}{\partial\phi^2} + \frac{1}{Z}\frac{\partial^2 Z}{\partial z^2} + \omega^2\mu_0\epsilon_0 = 0 \quad (2.23)$$

the expression for each field component of a TE cylindrical waveguide mode can be found from Eq. (2.21) and (2.22)

$$E_\rho = jE_1\frac{m}{k_\perp\rho}J_m(k_\perp\rho)e^{-jm\phi}f(z)$$

$$E_\phi = E_1J'_m(k_\perp\rho)e^{-jm\phi}f(z)$$

$$E_z = 0$$

(2.24)

$$H_\rho = -jE_1\frac{1}{\omega\mu_0}j'_m(k_\perp\rho)e^{-jm\phi}f'(z)$$

$$H_\phi = -jE_1\frac{m}{\omega\mu_0k_\perp\rho}j_m(k_\perp\rho)e^{-jm\phi}f'(z)$$

$$H_z = -jE_1\frac{k_\perp}{\omega\mu_0}j_m(k_\perp\rho)e^{-jm\phi}f(z)$$

(2.25)

From the boundary conditions $E_\phi = 0$ and $H_\rho = 0$, which yields the following expression for the transverse wavenumber

$$k_\perp = \frac{v'_{mn}}{a} = \frac{v'_{mn}}{r_{cavity}} \quad (2.26)$$

where a is radius of a cavity, n denote the radial mode number, v'_{mn} is the n th non vanishing zero of the derivative of the Bessel function $J'_m(x)$.

The modes in a cylindrical waveguide can be explained as a rays propagating tangentially to a cavity of caustic radius $r_{caustic}$ and Brillouin angle θ_B

$$r_{caustic} = \frac{m}{k_\perp} = r_{wg} \left(\frac{m}{v'_{mn}} \right)$$

$$\theta_B = \arcsin \left(\frac{k_\perp}{k} \right)$$

(2.27)

Which can be approximated as $\theta_B = \arcsin(r_{cavity} / r_{wg})$.

Chapter 3

Design and experiment of a mode generator

3.1 Design and experiment of a corrugated feed horn

A mode generator device uses a gaussian-like beam of the corrugated feed horn. It excites a mixture of TE_{11} and TM_{11} mode content which has an E-field distribution similar to the HE_{11} mode and forms Gaussian-like beam. A corrugated feed horn is consistent up to 98.1% efficient with a fundamental Gaussian beam.

For low loss transmission, the desired operating mode of corrugated waveguide is the HE_{11} mode [26, 27]. It is a linearly polarized HE_{11} mode in the waveguide which has a corrugation depth of $\lambda/4$. The final mode in free space is formed to be a Gaussian-like mode.

Mode conversion TE_{11} to HE_{11} of corrugated feed horn can be done using a smooth depth transition from $\lambda/2$ to $\lambda/4$ [28-35].

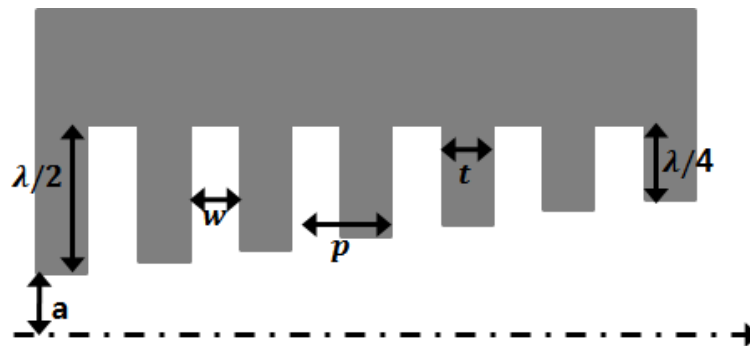


Figure 3-1: Schematic of a corrugated waveguide

p, w, d and a represent the corrugation period, the slot width, corrugation depth and the waveguide radius, respectively as shown in Figure 3-1. The frequency for the simulation is set to be at W-band where geometrical parameters such as depth (d), pitch (p), width (w) and thickness (t) defined have chosen accordingly as. $d = \lambda/4$, $t = \lambda/6$, $w = \lambda/3$ [36, 37].

After measuring beam generated from corrugated feed horn, we compared with simulation results obtained by HFSS program. The figure 3-2 is a corrugated feed horn.

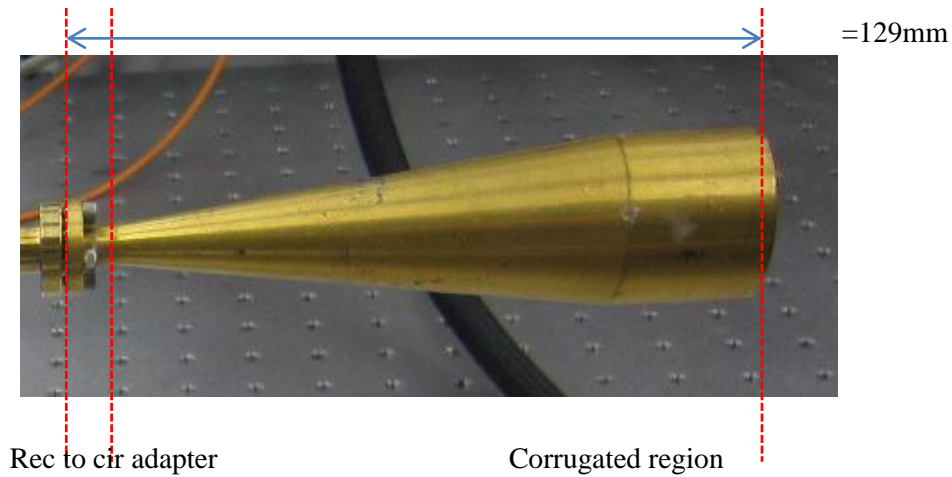


Figure 3-2: Corrugated feed horn (WR-08)

Circular corrugated horn is shown in figure 4.4. The inner surface of the waveguide is repeated periodically by an array of corrugated structure. Typically a $\lambda/4$ uniformly corrugated tapered section is attached at the end of the $\lambda/2$ to $\lambda/4$ transition. The effect on the attachment of the $\lambda/4$ corrugated tapered section was investigated and the geometry considered in the simulation is shown in Fig. 3-3 [38, 39].

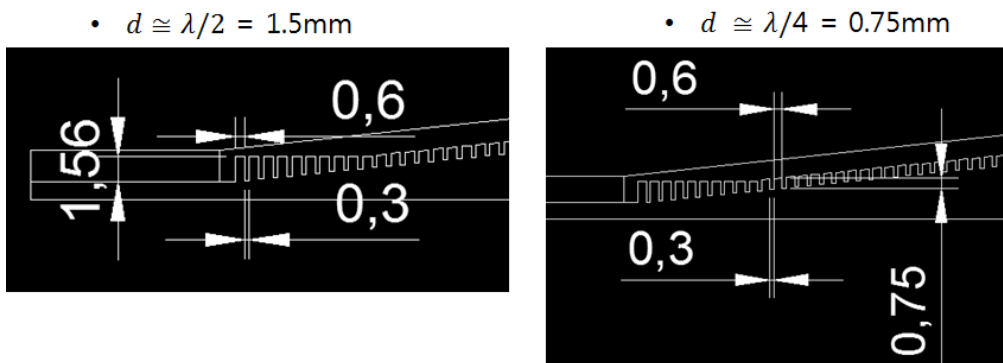


Figure 3-3: 95GHz corrugated horn.

Based on this, the entire length of corrugated feed horn is 129mm and radius at horn aperture is 16mm [40].

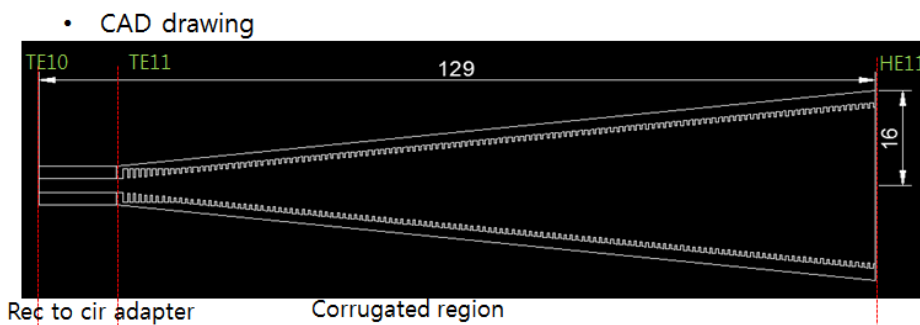


Figure 3-4: The structure of 95GHz corrugated horn.

Based on this, the E-field pattern is confirmed by HFSS program. Due to limited computer resources (Table 3-1) and run-time, we used symmetry of the structure

	Simulation computer
OS	Window7 Professional
CPU	I7 870
RAM	10.0 GB

Table 3-1: Computer resources of corrugated feed horn simulation

Table 3-2 shows the parameter setting for HFSS simulation. The entire structure was set aluminum and using wave-port of the excitation and a symmetry boundary structure. The entire structure of the horn simulation is 118×1×32mm.

	Set up of a simulation
Simulation program	HFSS
Solution Type	Driven Modal
Frequency	95GHz
Excitations	Wave port
Boundary	Symmetry Boundary
Material	Aluminum
Boundary Size	118×1×32mm

Table 3-2: The parameter setting for horn simulation.

The simulation results of the E-field pattern were confirmed. An electric beam pattern is converted from HE_{11} mode to Gaussian-like beam pattern at the horn aperture which is confirmed by simulation results.

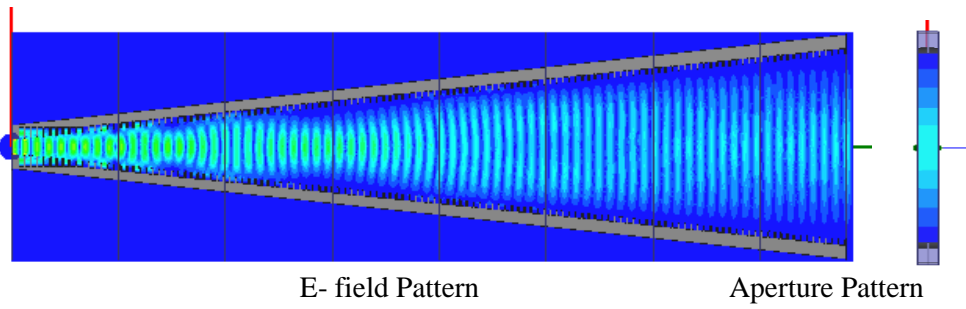


Figure 3-5: Simulation results of the corrugated feed horn (E field pattern).

In order to check the simulation result, the field pattern from the horn antenna was measured. Figure 3-6 is an experimental setup for measuring the horn using VNA. An Agilent PNA-X N5247A was connected to W-band corrugated feed horn and open-cut waveguide probe. Also, we used a xyz scanning device made by MTG Corp. If we want to measure the beam properties, x, y axis were measured at certain resolution. And the distance between horn and open waveguide was measured by the z axis.

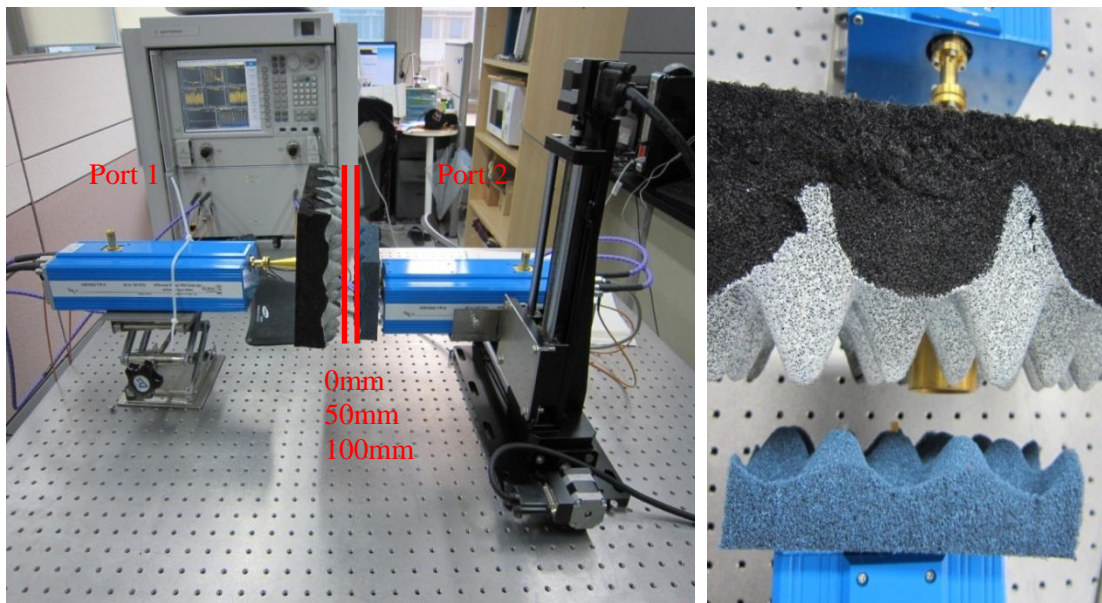


Figure 3-6: Experimental environment for the horn.

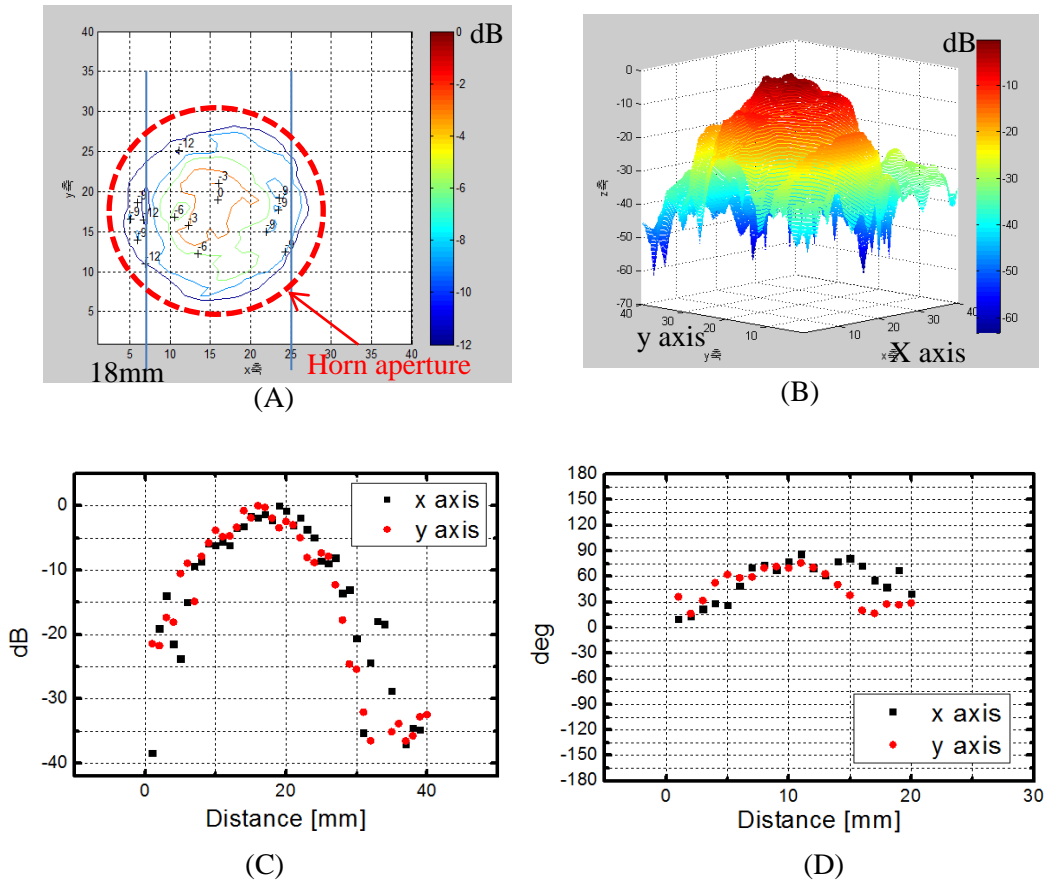


Figure 3-7: Experimental results of 0mm distance from a horn aperture to open-cut waveguide.
 (A) Amplitude plot by 12dB (B) 3D amplitude plot (C) 1D amplitude plot (D) 1D phase plot

The Fig. 3-7 is experimental results of 0mm distance from a horn aperture to open-cut waveguide. If the distance changes at z axis, the beam characteristics can be measured by VNA. So, we changed the z axis and measured. The red color represents the calculated beam size by 8.7dB. Fig. 3-7(A) shows a gaussian-like beam amplitude by 12dB. Fig. 3-7(C) shows a gaussian-like beam amplitude expressed as 1D. Fig. 3-7(D) shows a Gaussian-like beam phase expressed as 1D.

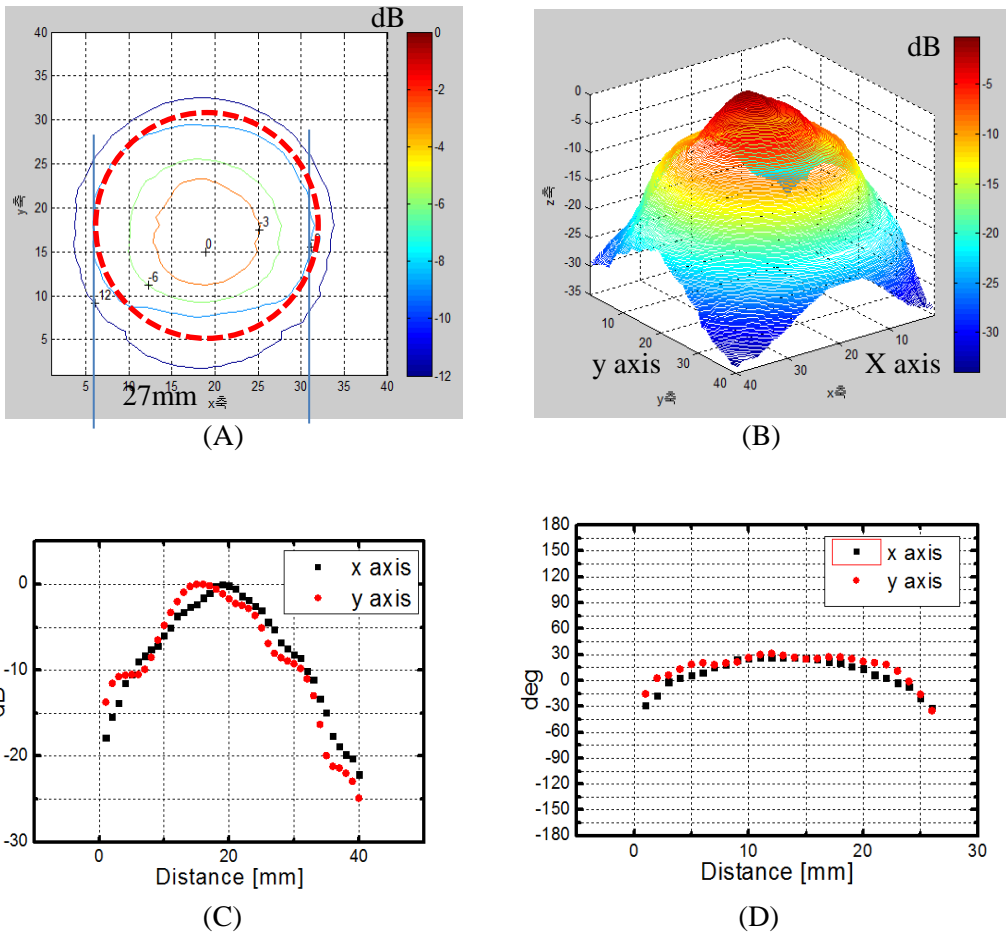
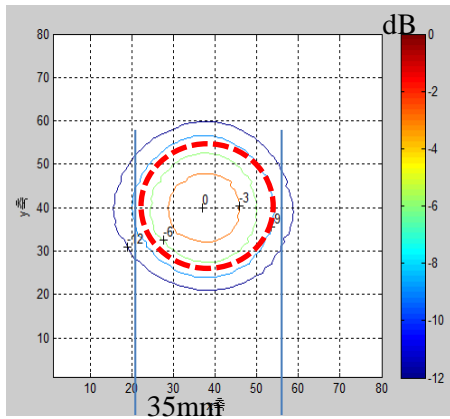
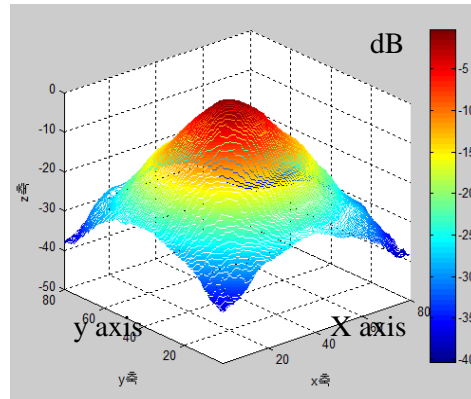


Figure 3-8: Experimental results of 50mm distance from a horn aperture to open-cut waveguide.
 (A) Amplitude plot by 12dB (B) 3D amplitude plot (C) 1D amplitude plot (D) 1D phase plot

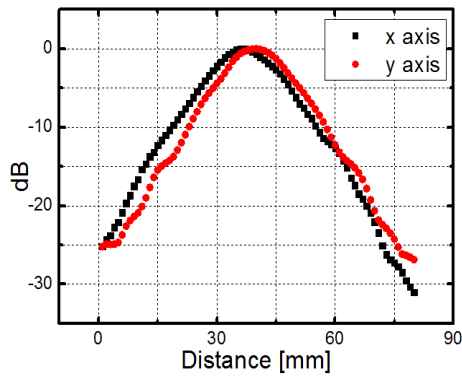
The Fig. 3-8 is experimental results of 50mm distance from a horn aperture to open-cut waveguide. The red color represents the calculated beam size by 8.7 dB. Fig. 3-7(A) shows a gaussian-like beam amplitude by 12dB. Fig. 3-7(C) shows a gaussian-like beam amplitude expressed as 1D. Fig. 3-7(D) shows a Gaussian-like beam phase expressed as 1D. In the case of 50mm distance, the cavity was designed to be located.



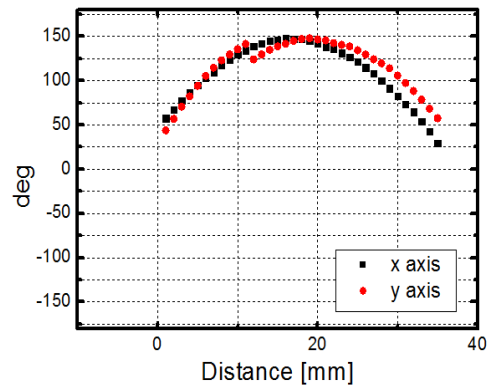
(A)



(B)



(C)



(D)

Figure 3-9: Experimental results of 100mm distance from a horn aperture to open-cut waveguide.

(A) Amplitude plot by 12dB (B) 3D amplitude plot (C) 1D amplitude plot (D) 1D phase plot

The Fig. 3-9 is experimental results of 100mm distance from a horn aperture to open-cut waveguide. As shown in the Fig. 3-7, 3-8, and 3-9, we found good agreement between the measurement results and calculation data.

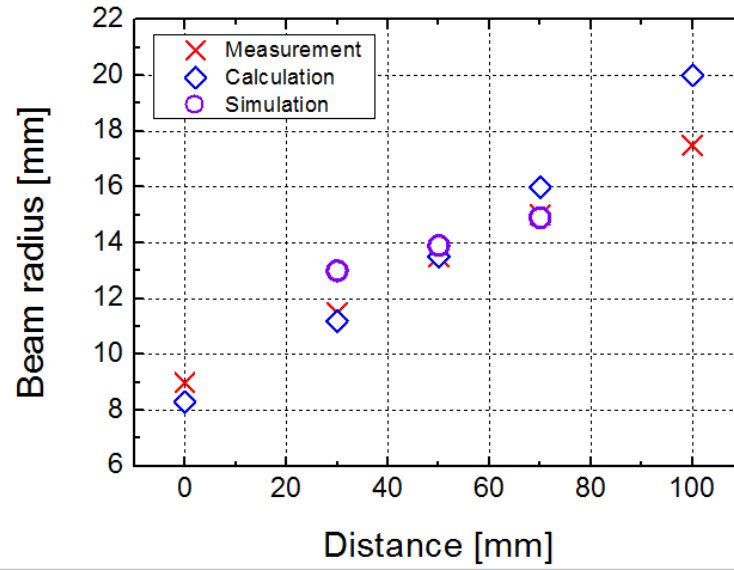


Figure 3-10 Data comparison plots of measurement, calculation and simulation results. It is propagated from corrugated feed horn.

$$W(z) = W_0 \left[1 + \left(\frac{\lambda z}{\pi W_0^2} \right)^2 \right]^{0.5} \quad (3.1)$$

Equation 3.1 is Gaussian beam equation. Where $W(z)$ is the radius after the wave has propagated a distance z , W_0 is the radius of the $1/e^2$ where wavefront is flat and z is the distance propagated from the plane the distance.

We confirmed Gaussian-like beam through measured horn data. The figure 3-10 describes measurement results of beam size that propagated from corrugated feed horn. Experimental beam size shows a good agreement to the simulation result. Based on this, one can confirm that the expected beam size is going to be injected to the cavity.

3.2 Design and experiment of a mirror

Quasi-optical analysis has been done for designing mirror structures [41]. Parameters for mirror structures have been extracted and the design parameters were validated using a commercial finite element code, High Frequency Structure Simulator (HFSS).

The mirrors are either parabolic shape or elliptical shape in perpendicular and parallel direction

with respect to the beam propagation direction. Each directional component has been analyzed separately to determine Gaussian beam size as the beam propagates.

We compared measurement data with results of simulation using HFSS program. We have designed that Gaussian beam is supposed to inject the cavity. To do so, we must control the gaussian beam using mirrors.

As shown in the figure 3-11, the beam waist from the corrugated feed horn is 6 mm(radius). The coupling holes of a cavity are 10×20 mm in size. Based on Section 2.2, we have designed mirrors. It consists of parabolic share and elliptical shape.

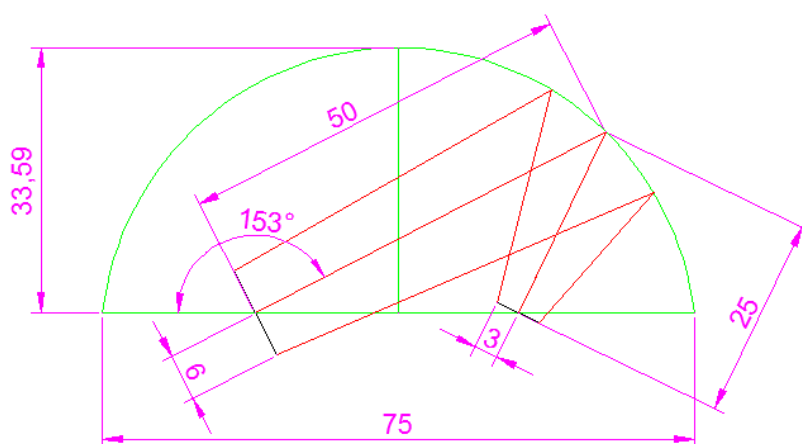


Figure 3-11: The design drawing of a parabolic mirror

W in	W out	Z	focal F	R1(=din)	R2(=dout)	Ao	Angle
6.00	5.65	9.00	25.00	50.00	50.00	50.00	120.00
6.00	3.69	9.00	21.39	55.00	35.00	42.78	140.48
6.00	2.90	9.00	16.67	50.00	25.00	33.33	153.62

Table 3-3: The calculation of parabolic mirror.

The beam size located inner cavity is 2.9mm (radius). It enters to the cavity by ray optics. As based on the parameters of mirrors, mirrors are designed by HFSS software.

Due to limited computer resources and run-time, we used limited geometrical size by applying symmetry.

Table 3-6 shows the parameter setting for HFSS simulation. The entire structure was set aluminum and using Gaussian beam of the excitation and a radiation boundary structure. The entire structure of

the mirror simulation is 58×25×3mm.

Frequency	95 GHz
Excitations	Gaussian beam
Mesh size	0.6667 Lambda
Boundary	Radiation field
Boundary size (x,y,z)	58×25×3 (mm)
Material	Aluminum

Table 3-4: The parameter setting for horn simulation.

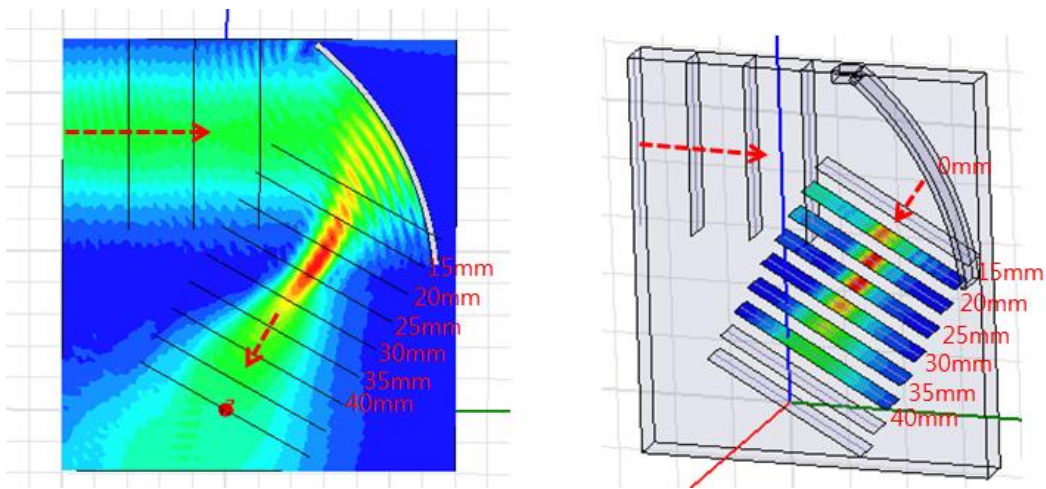


Figure 3-12: Simulation results on E-field pattern at mirror.

Figure 3-12 is the result of the simulation. A beam reflected by mirror propagates into the cavity, and we want to control desired beam size. The beam size of 25mm from reflected mirror is simulated to be the smallest. Figure 3-13 shows the simulation results by distance.

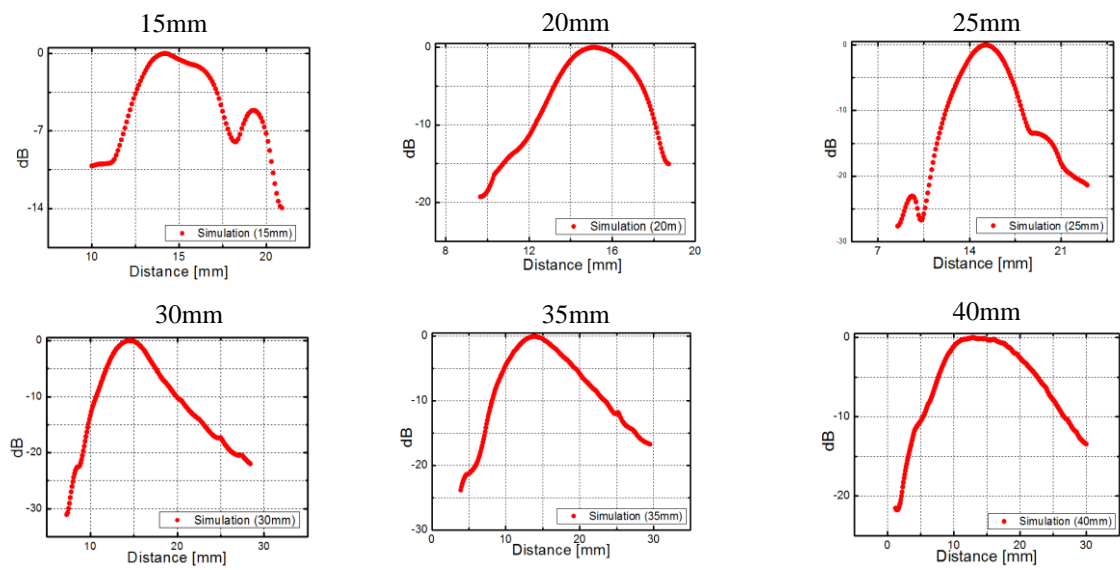


Figure 3-13: 1D amplitude plot of mirror simulation from reflected mirror

The beam size was measured for comparing to simulation results. Figure 3-13 is an experimental environment for measuring the mirror and an experimental environment for measuring the horn using VNA on S-parameter.

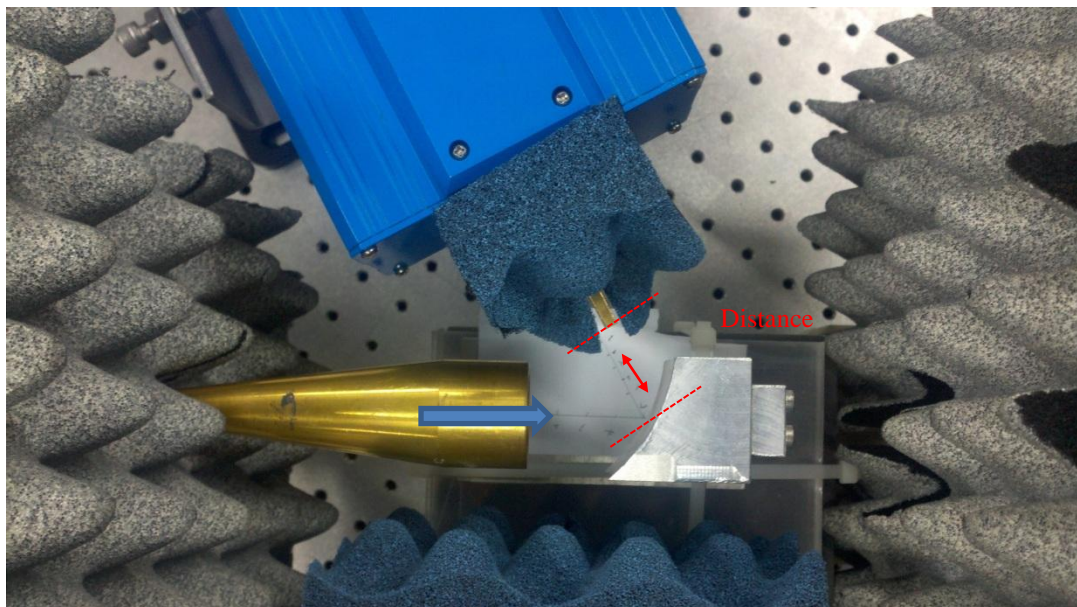
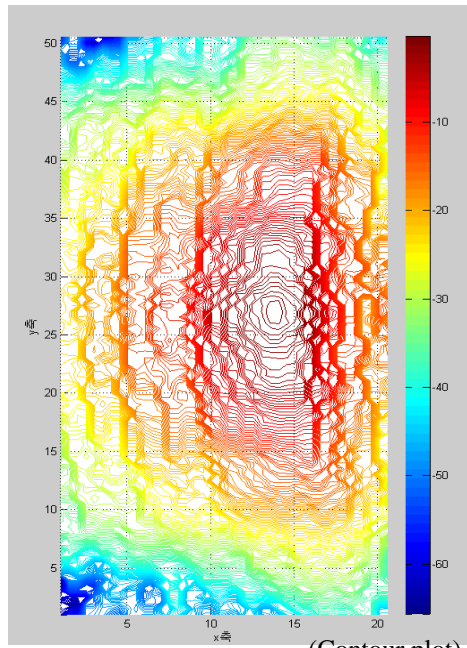


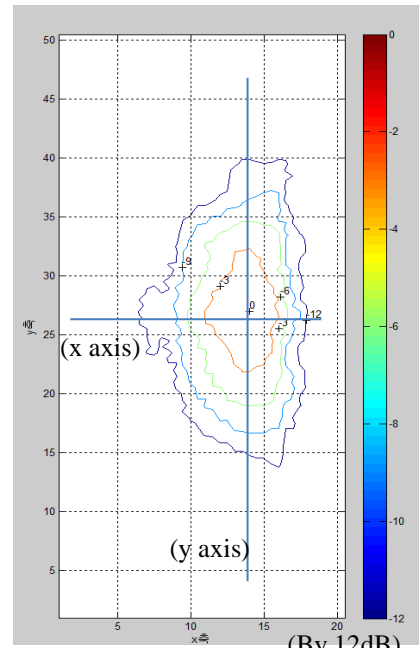
Figure 3-14: Experimental environment of reflected beam from mirror.

1D plot of the high intensity showed picture 3-15, 3-16, and 3-17. One can check measurement results such as elliptical mirror of x axis and parabolic mirror of y axis.

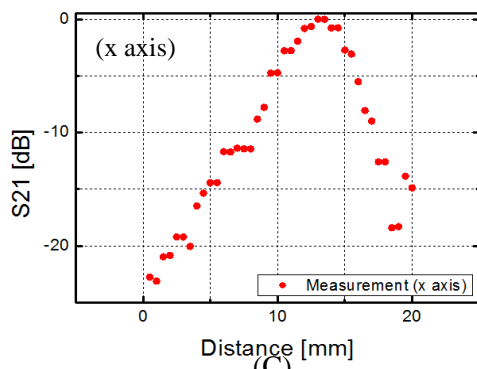
The Fig. 3-15, 3-16, and 3-17 are experimental results of 15, 20, and 25 mm distance from reflected mirror to open-cut waveguide. The red color represents the calculated beam size by 8.7 dB. Fig. 3-15(A) shows contour plot of 2D beam amplitude by 12dB. Fig. 3-15(B) shows a beam amplitude expressed as 2D by 12dB. Fig. 3-15(C) shows 1D amplitude plot of the high intensity at the x axis. Fig. 3-15(D) shows 1D amplitude plot of the high intensity at the y axis. Fig. 3-15(E) shows 1D phase plot of the high intensity at the x and y axis.



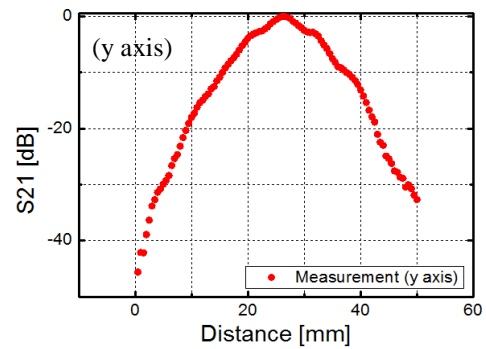
(A) (Contour plot)



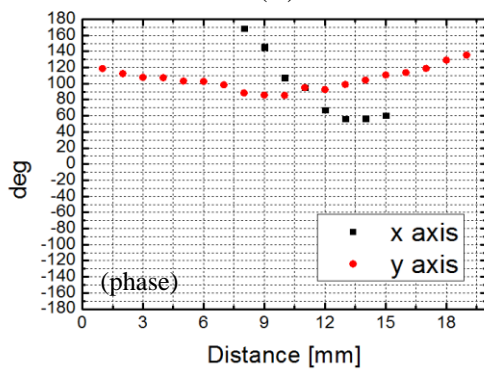
(B) (By 12dB)



(C)



(D)



(E)

Figure 3-15: Experimental results of 15mm distance from reflected mirror to open-cut waveguide.

(A) 2D amplitude plot (B) Amplitude plot by 12dB (C) 1D amplitude plot of x axis (D) 1D amplitude plot of y axis (E) 1D phase plot

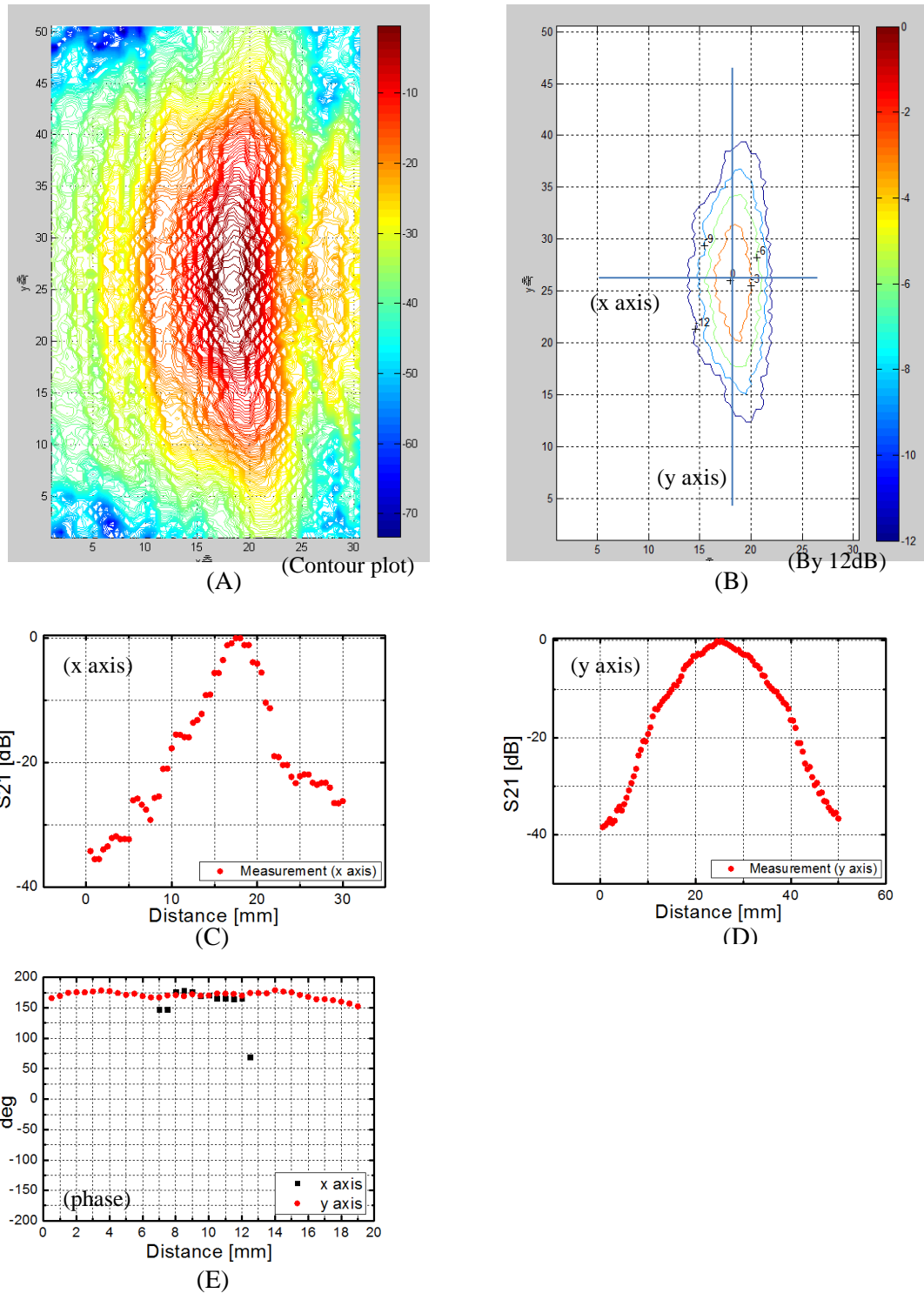


Figure 3-16: Experimental results of 20mm distance from reflected mirror to open-cut waveguide.

(A) 2D amplitude plot (B) Amplitude plot by 12dB (C) 1D amplitude plot of x axis (D) 1D amplitude plot of y axis (E) 1D phase plot

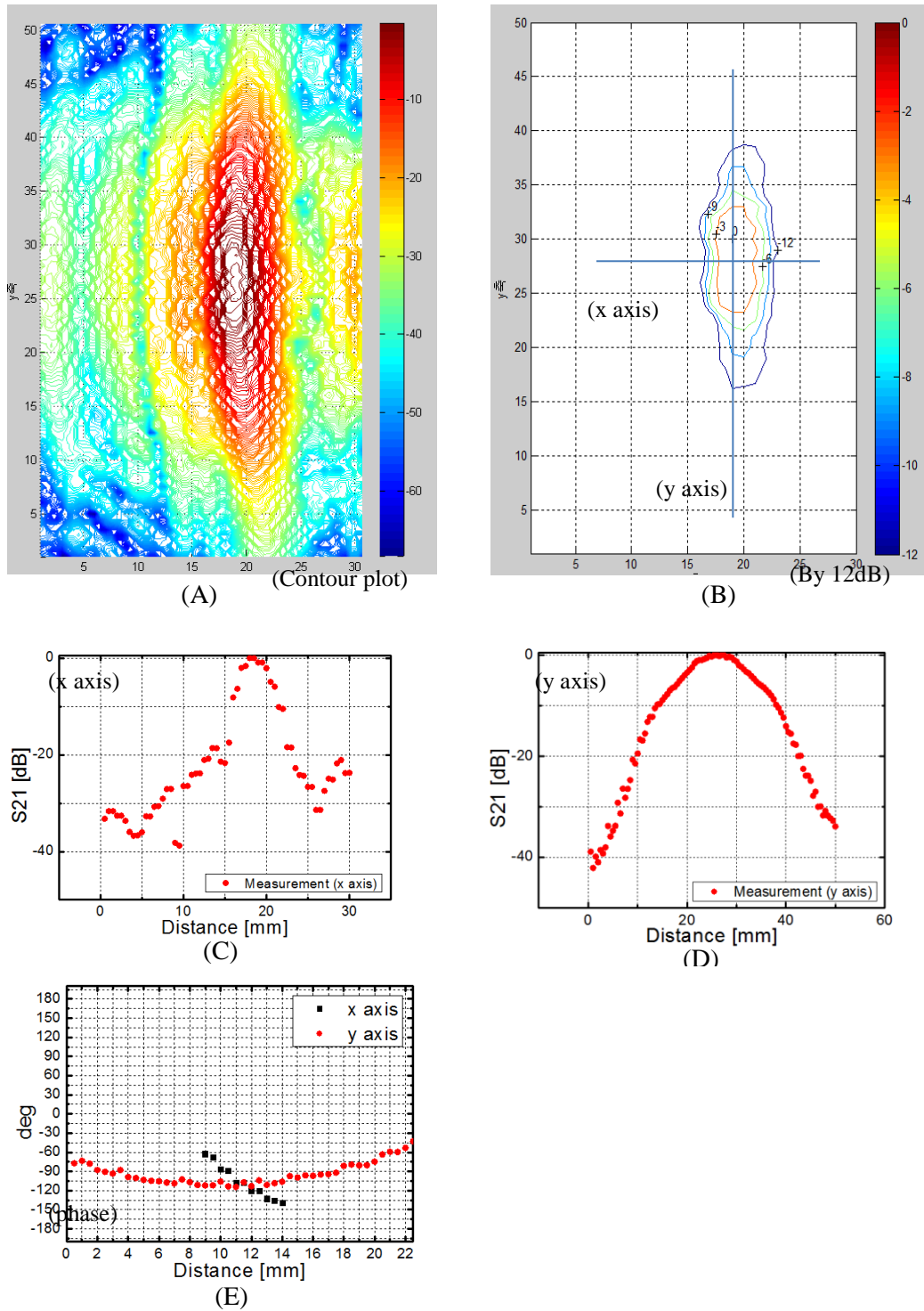


Figure 3-17: Experimental results of 25mm distance from reflected mirror to open-cut waveguide.

(A) 2D amplitude plot (B) Amplitude plot by 12dB (C) 1D amplitude plot of x axis (D) 1D amplitude plot of y axis (E) 1D phase plot

As shown in Fig. 3-17(B), the desired beam is injected into the cavity. According to measured results in figure 3-15, 3-16, and 3-17, we were compared with calculated data. Figure 3-18 describes the beam size reflected from a mirror to cavity. Controlled Beam propagates to the cavity. Each directional component has been analyzed separately to determine the gaussian beam size as the beam propagates. The measurement results of beam reflected from mirror are in good agreement with calculations and simulations.

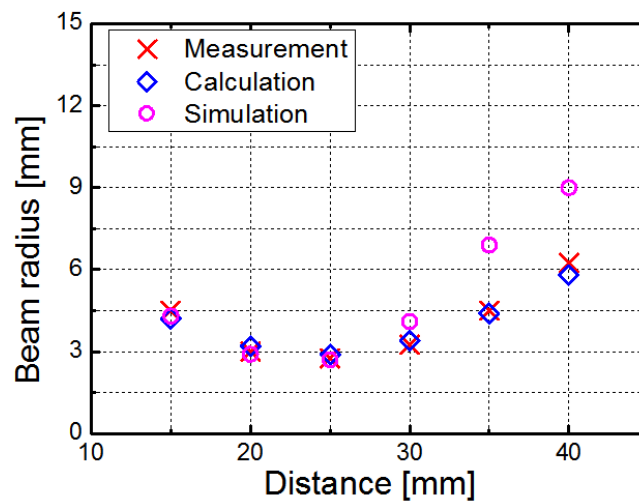


Figure 3-18: Data comparison plots of measurement, calculation and simulation results. It is propagated from reflected mirror.

We compared measurement data with results of simulation. The measurement results of beam reflected from mirror are in good agreement with calculations and simulations.

3.3 Design and experiment of a cavity

The beam is injected into the hole of cavity structure. The injected beam can interpret as plane wave. This can have two different interpretations. Firstly, the beam progress along the caustic of cavity and rotates according to Aximuthal bounce angle. Secondly, the propagating beam is supposed to follow Brillouin angle. The cavity must create TE mode of desired pattern. Table 10 shows the design parameter of the cavity.

Operating Mode	TE_{62}
Waveguide radius r_{cavity}	6 mm
Waveguide radius r_{wg}	7 mm
Caustic radius $r_{caustic}$	3 mm
Brillouin angle θ_B	60°
Bounce angle ψ	60°

Table 3-5: Design parameter of the cavity.

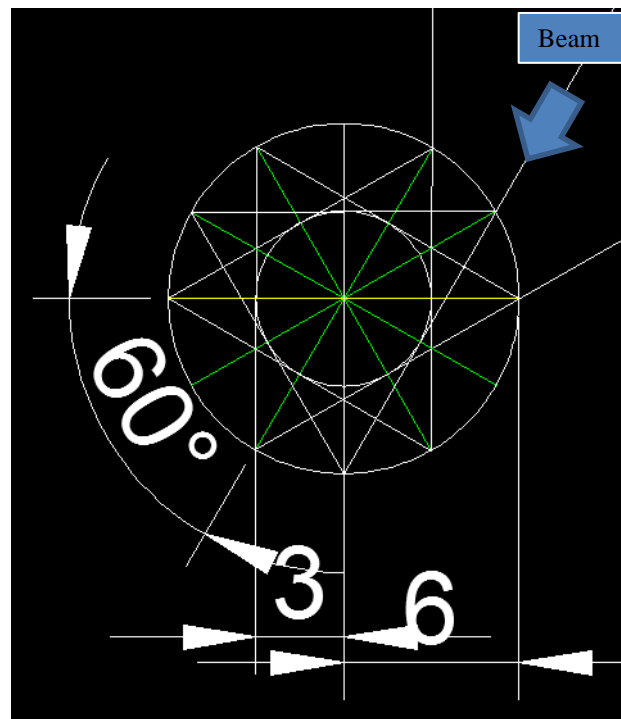


Figure 3-19: Geometrical optics view of a cylindrical waveguide

The inner metal rod was inserted to control desirable mode [42].

The cavity aperture of up taper section is 14 mm. it can be divided into two kinds of reasons. Firstly, the aperture of cavity is larger, the measurement of the beam pattern at the aperture would be easier. Secondly, one can test the launcher and mode converter system by directly attaching the cavity.

The cavity is usually a nonlinear taper cylindrical waveguide structures as shown in the figure 3-20. The input part of down taper is a cut off section, which blocks the back propagation of beam.

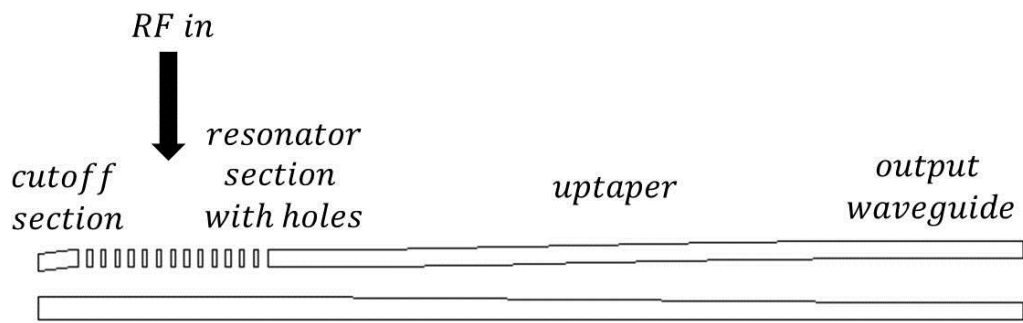


Figure 3-20: Schematic of coaxial cavity [3] .

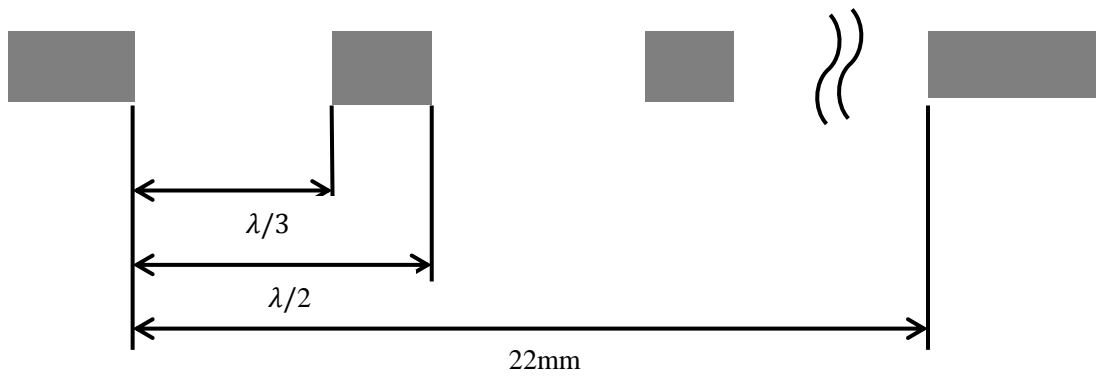


Figure 3-21: Schematic of holes on coaxial cavity wall. The section consists of 15 axially \times 25 azimuthally.

The requirements to provide good coupling are chosen by the diameter of the holes and the thickness of the wall. We have made holes consist of 15(axially) \times 25 (azimuthally). The wall with a thickness of 0.2mm is made, and the size of the holes is $\lambda/3$ diameter.

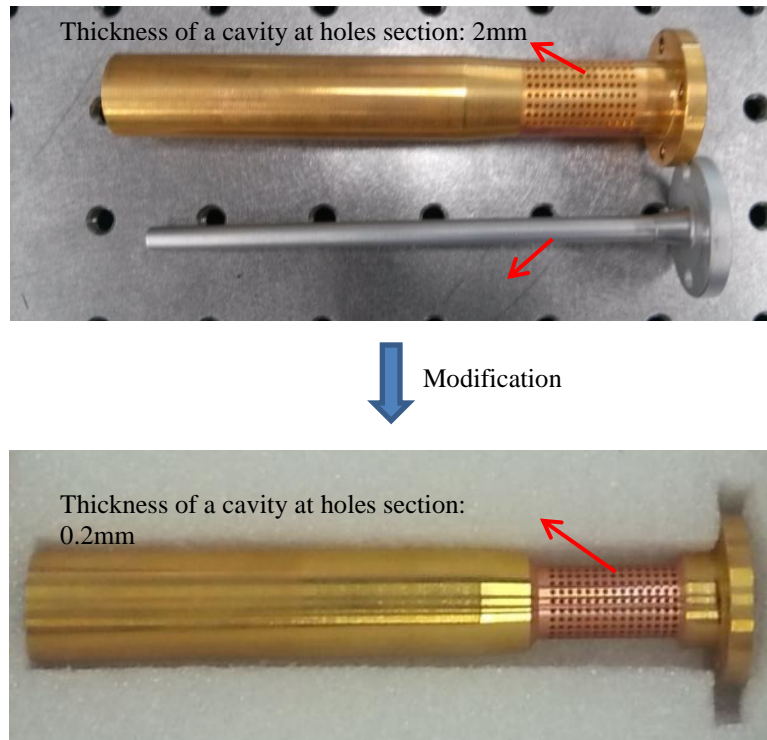
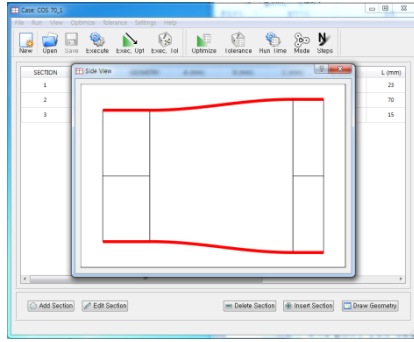


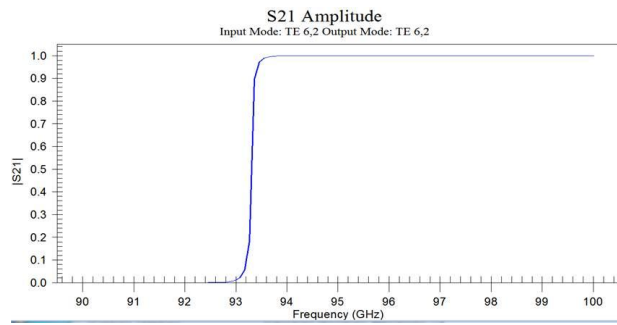
Figure 3-22: The picture of the coaxial cavity. Due to good coupling, the cavity thickness changed from 2mm to 0.2mm.

We had to change the thickness from 2mm to 0.2mm because of the coupling. The thickness of 0.2mm occurs good-coupling. We learned through experimentation. Figure 3-22 is a modified cavity.

Due to complex structures of the cavity, we divided two kinds of simulations such as up taper section and coupling simulation. The first simulation is CASCADE code. The commercial software, CASCADE code, has implemented the briefly mentioned mode matching technique with the scattering matrix formulation [43, 44]. We used the CASCADE for obtaining scattering parameters in a waveguide. The cavity can create neighboring modes while passing through the taper section. In order to prevent other modes, we designed optimized tapered section. We achieved almost 100% purity through CASCADE code.



(A)



(B)

Figure 3-23: CASCADE Code Simulation. (a) CASCADE View (b) S21 Amplitude TE_{62} mode

S21 Amplitude	TE_{62}
TE_{61}	$8.1 \times 10^{-5} \%$
TM_{61}	$1.67 \times 10^{-4} \%$
TE_{62}	99.99 %
TM_{62}	$4.9 \times 10^{-5} \%$

Table 3-6: Simulation results of CASCADE Code (Input mode: TE_{62} mode).

The hole structure of cavity is difficult to analyze than previous simulations. The second simulation using HFSS program analyzed coupling interpretation. In order to interpret the complex structures, we used a 128 RAM memory workstation. The run-time of simulation analysis took 43hours. Based on this, the E-field pattern is confirmed by HFSS program. Table 3-7 is the parameter setting for horn simulation.

Frequency	95 GHz
Excitations	Waveguide port
Mesh size	0.6667 Lambda
Boundary	Symmetry Boundary
Boundary size (x,y,z)	16 * 14 *20 (mm)
Material	Aluminum
Run time	43 hour

Table 3-7: Simulation set-up of hole structure cavity using waveguide port.

Simulation computer resources	
OS	Win7 Professional 64bit
CPU	I7 870
RAM	128 GB

Table 3-8: Computer specification for simulation of coupling.

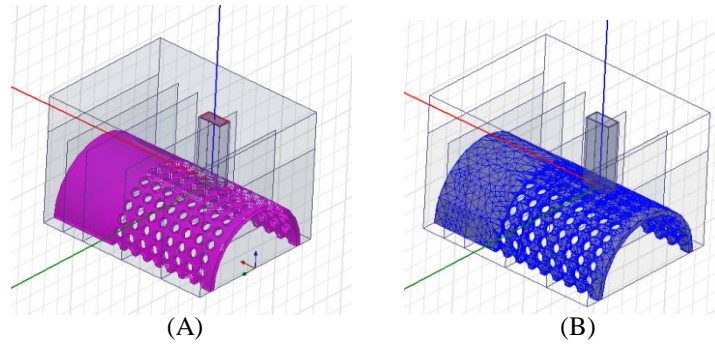


Figure 3-24: Simulation set-up for a hole structure cavity using HFSS program (a) Excitation view (b) Mesh set-up: 0.6667 Lambda

Through this simulation, we confirmed TE_{62} mode pattern from the aperture of the cavity. Figure 3-25 is results of the coupling simulation. We saw TE_{62} mode at number 4 in figure 3-25. A short length of the entire structure had confirmed that desired pattern was shown by simulation. Base on this simulation, we made a cavity.

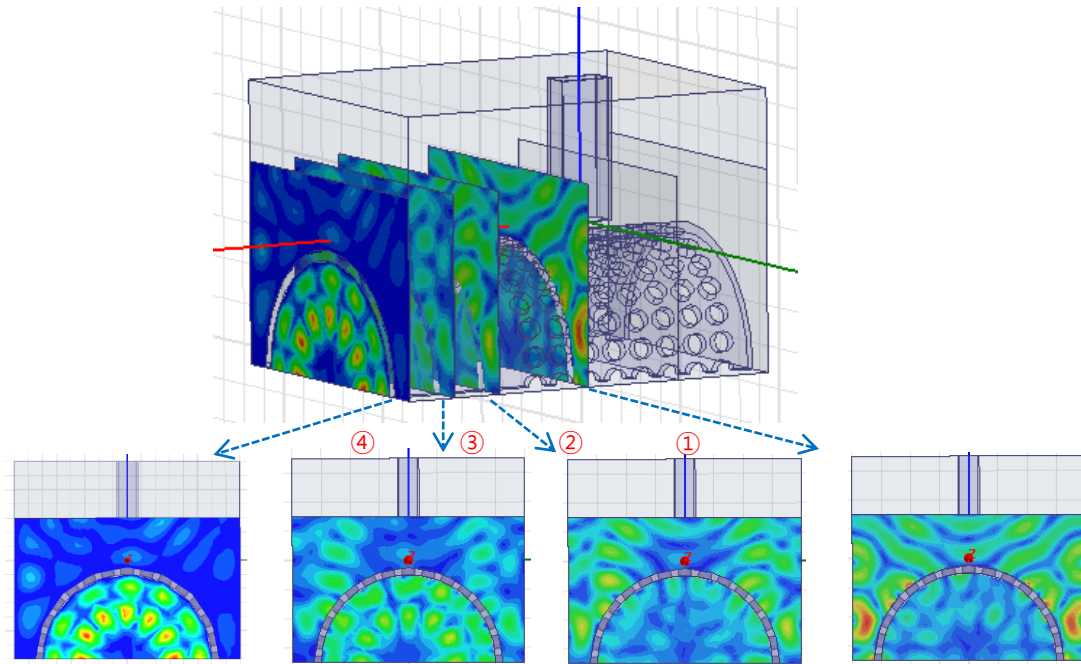


Figure 3-25: Coupling simulation of a cavity using HFSS program (E-field pattern)

We confirmed E- field patterns of x axis and y axis using CST program. Figure 3-26 shows the simulation results of each direction. The measurement results were determined by comparing CST simulations. Figure 3-26 (C) shows the pattern of the TE_{62} mode. In the case of the simulation, we were easy to see the desired mode. However, in the case of actual measurement for a mode generator, we had to consider a lot of parts. The measurement is very sensitive on the experimental condition such as alignment, coupling of the cavity, and unwanted interception from reflected beams.

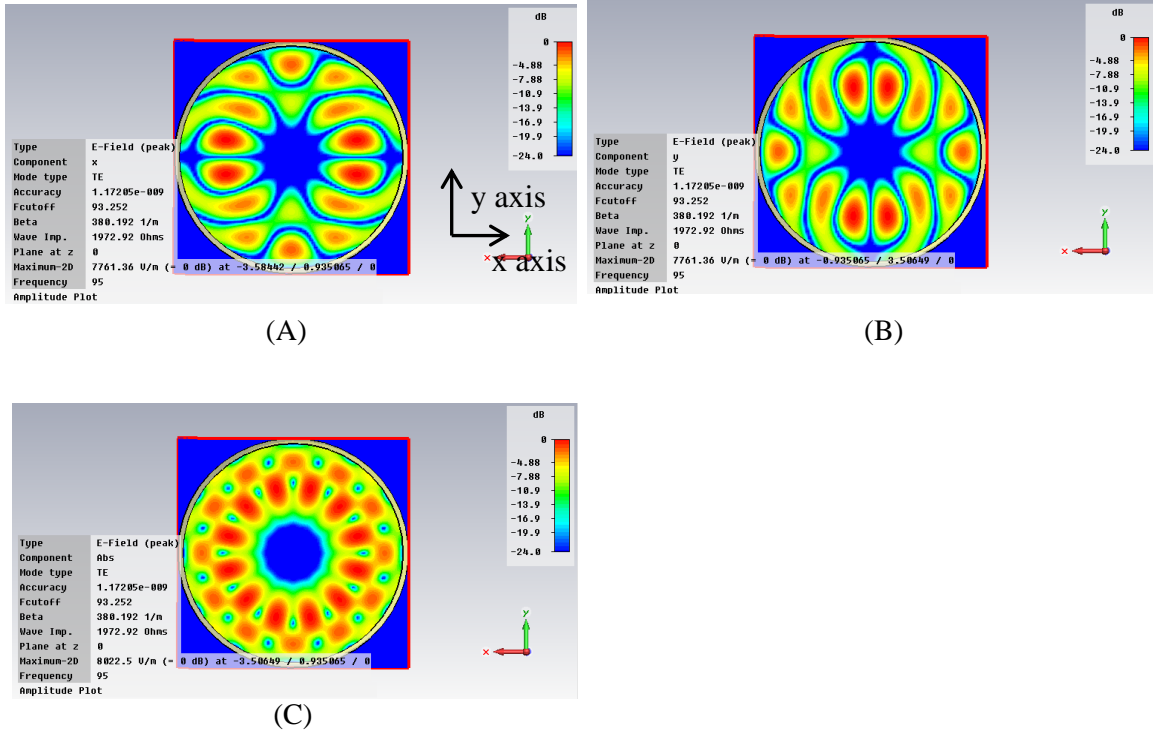


Figure 3-26: Simulation results of CST for pattern of each axis. (A) x-axis E-field pattern (B) y-axis E-field pattern (C) Sum E-field pattern

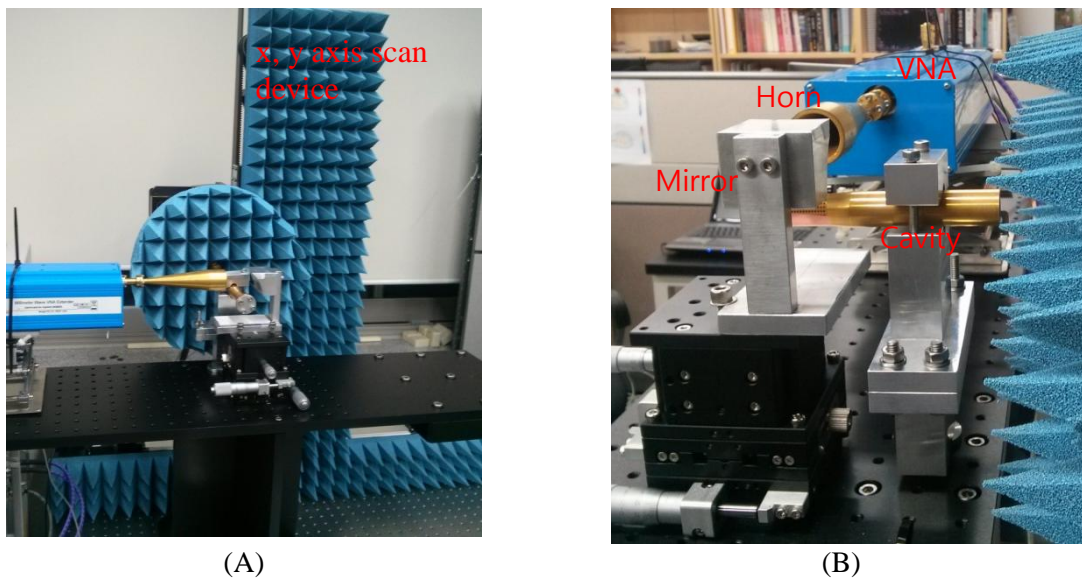


Figure 3-27: Experimental environment of a mode generator. (A) Experiment using scan device (B) A mode generator

3.3.1 Comparison between counter clockwise and clockwise

We designed the mode generator system and measured it. We wanted to find a way to get good measurement data. E-field pattern was measured by distance from aperture to open waveguide probe. When the incidence wave is injected on inner surface of the cavity, the results differ from the way it takes such as the counter clockwise or clockwise. We chose E-field pattern at the scan area.

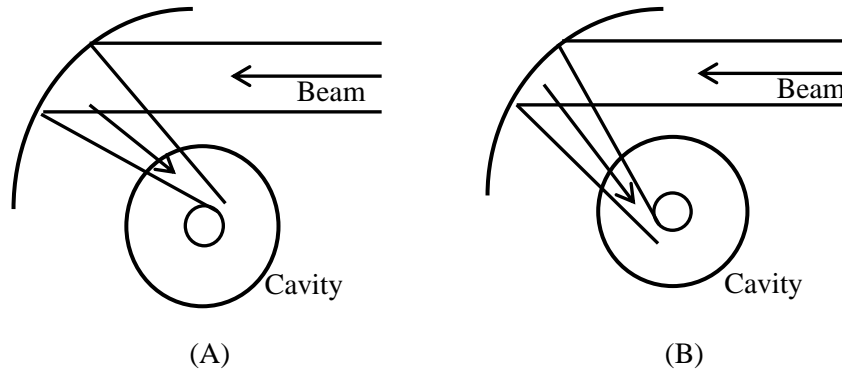


Figure 3-28: Propagating to cavity. (A) The counter clockwise (B) The clockwise

The scan area is 40×40mm. We measured S21 parameter at a 1.75 cm distance from aperture to open waveguide.

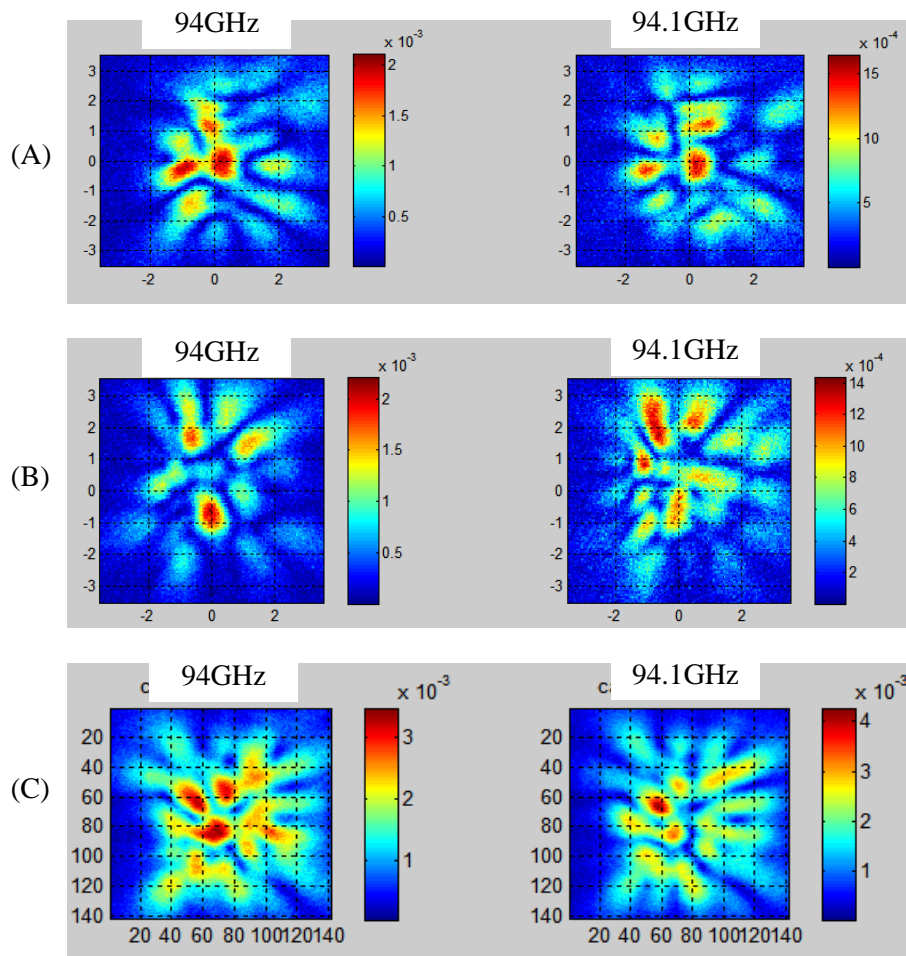


Figure 3-29: E-field Magnitude pattern of the counter clockwise. (A) The vertical axis (B) The horizontal axis (C) The sum of vertical and horizontal axis

Figure 3-29 is the E-field Magnitude pattern of the counter clockwise. We can not confirm that E-field pattern generate at the cavity. So, we were thinking the other way such as the inner rod. Figure 3-30 is the E-field Magnitude pattern of the clockwise and insertion of the inner rod.

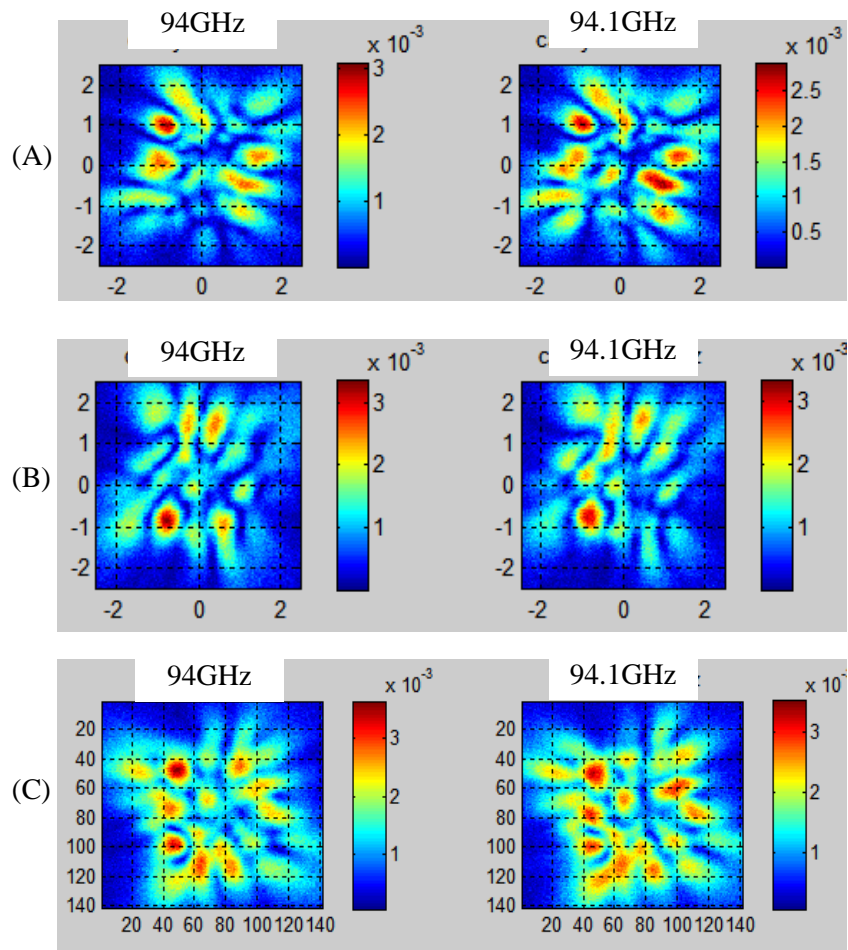


Figure 3-30: E-field Magnitude pattern of the clockwise and insertion of the inner rod. (A) The vertical axis (B) The horizontal axis (C) The sum of vertical and horizontal axis

Fig. 3-29 and Fig. 3-30 are measurement results for vertical and horizontal axis. The clockwise beam pattern is better than the counter clockwise beam pattern in the cavity. So we chose a measurement way of the clockwise. In other words, the counter clockwise at injected beam direction is better than the clockwise.

3.3.2 Inserting an inner rod in a cavity

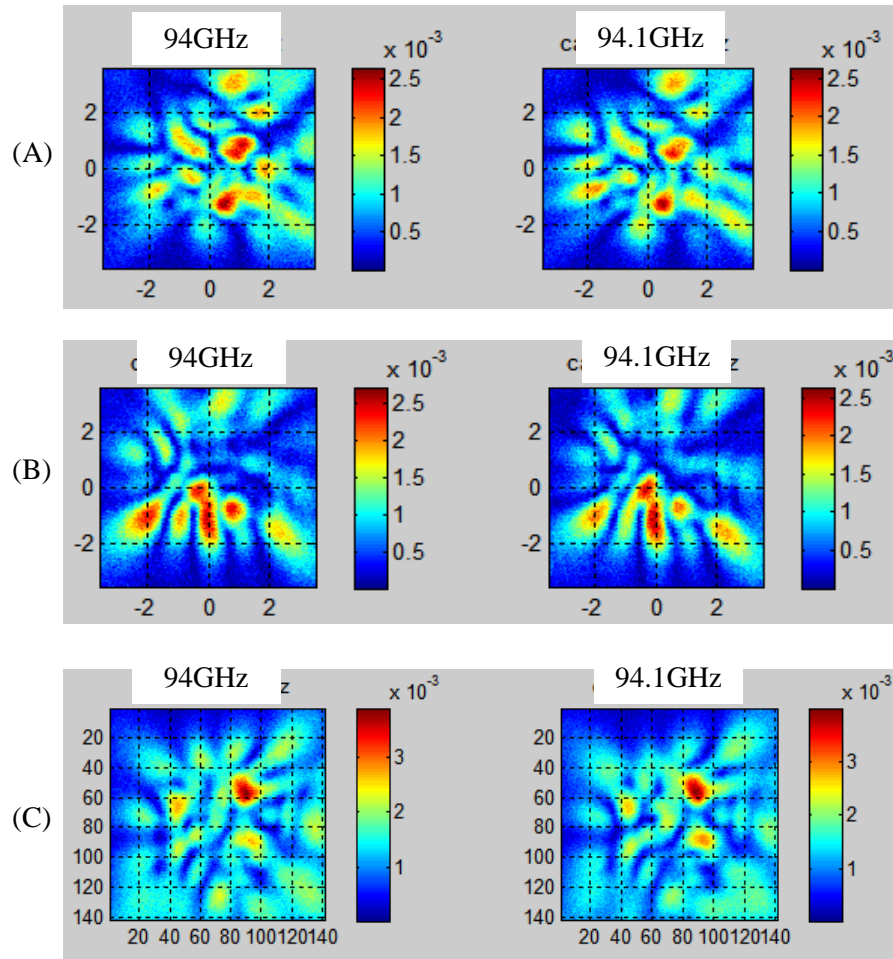


Figure 3-31: E-field Magnitude pattern of no insertion of the inner rod in the cavity. (A) The vertical axis (B) The horizontal axis (C) The sum of vertical and horizontal axis

As shown in Figure 3-30 and 3-31 we saw the results of the measurement. According to the effect of an inner rod, the measurement results were different. We thought that an inner rod is used in a coaxial cavity for improvement of the mode purity. The effects of the inner rod are shown in Fig. 3-30. The desired mode pattern did not occur. So, we had to look for another way. Fig. 3-32 is Modification of measurement environment such as absorber and arrangement.

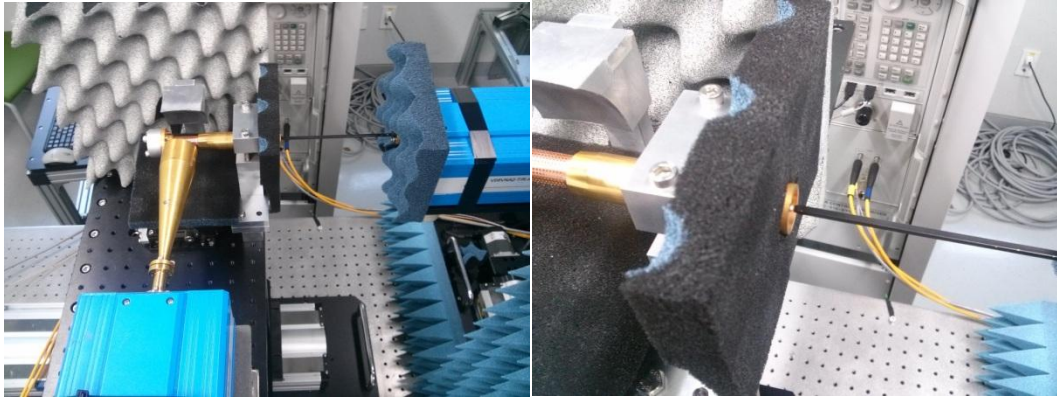


Figure 3-32: Modification of measurement environment such as absorber and arrangement.

3.3.3 Changing the measurement distance

The distance between the aperture of the horn and the probe was changed to as close as 1mm. And the beam absorber was carefully adjusted to avoid interference. The E-field distribution has been scanned directly at the output of the cavity in vertical polarization. The scanned area is 15×15 mm with 75×75 points of resolution. Figure 3-34 is 1mm distance measurement from aperture to open waveguide probe, the vertical E-field magnitude pattern. Figure 3-34 is 1mm distance measurement from aperture to open waveguide probe, the horizontal E-field magnitude pattern.

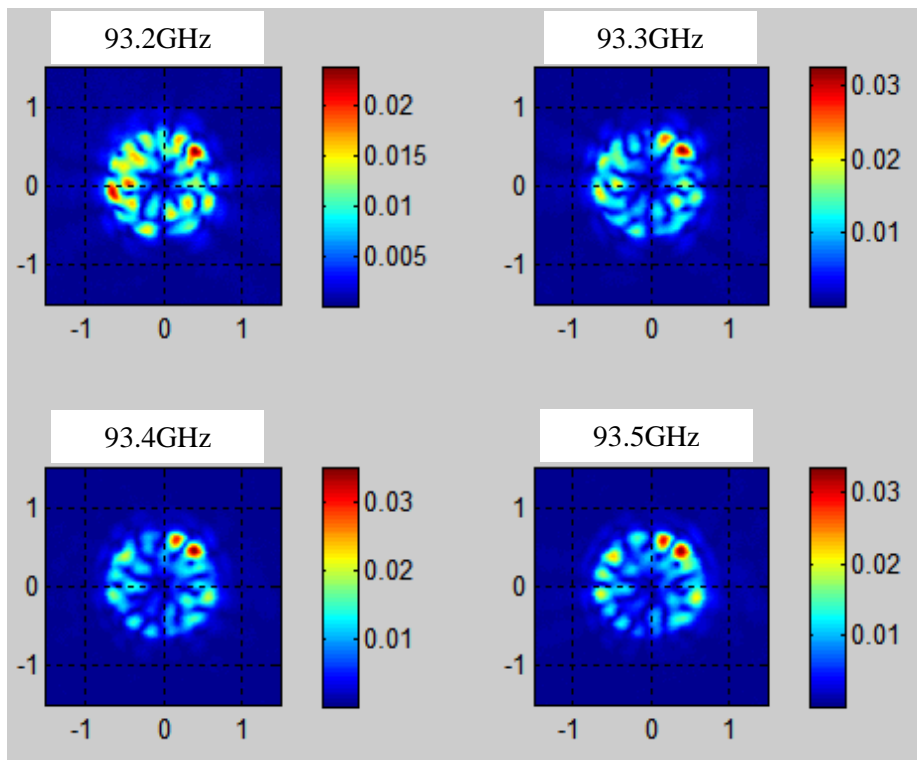


Figure 3-33: 1mm distance measurement from aperture to open waveguide probe, the vertical E-field magnitude pattern.

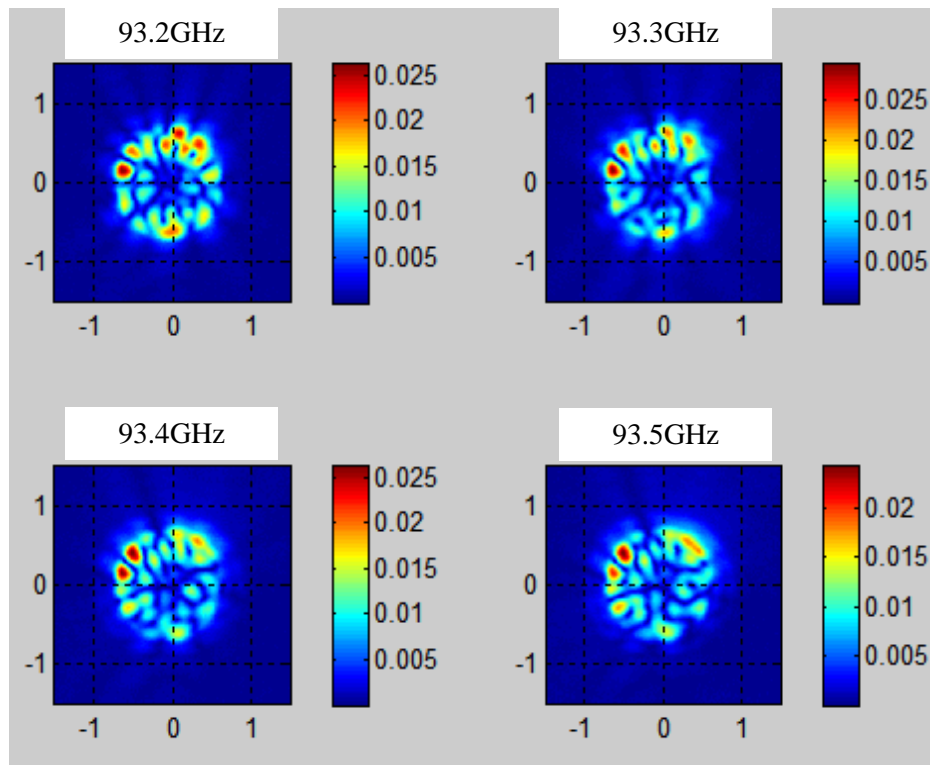


Figure 3-34: 1mm distance measurement from aperture to open waveguide probe, the horizontal E-field magnitude pattern.

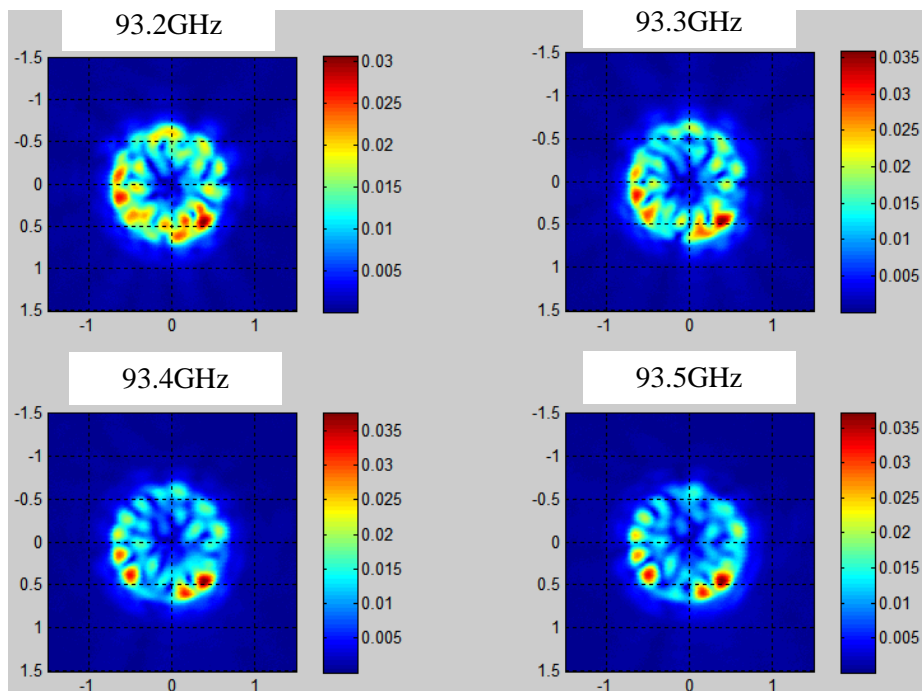


Figure 3-35: 1mm distance measurement from aperture to open waveguide probe. The sum of vertical and horizontal axis magnitude

This is shown in Fig. 3-35, where the sum of vertical and horizontal axis is plotted with respect to the distance of a cavity. The intensity is low at the inner rod position of the center, the radially axis is similarly the desired mode pattern.

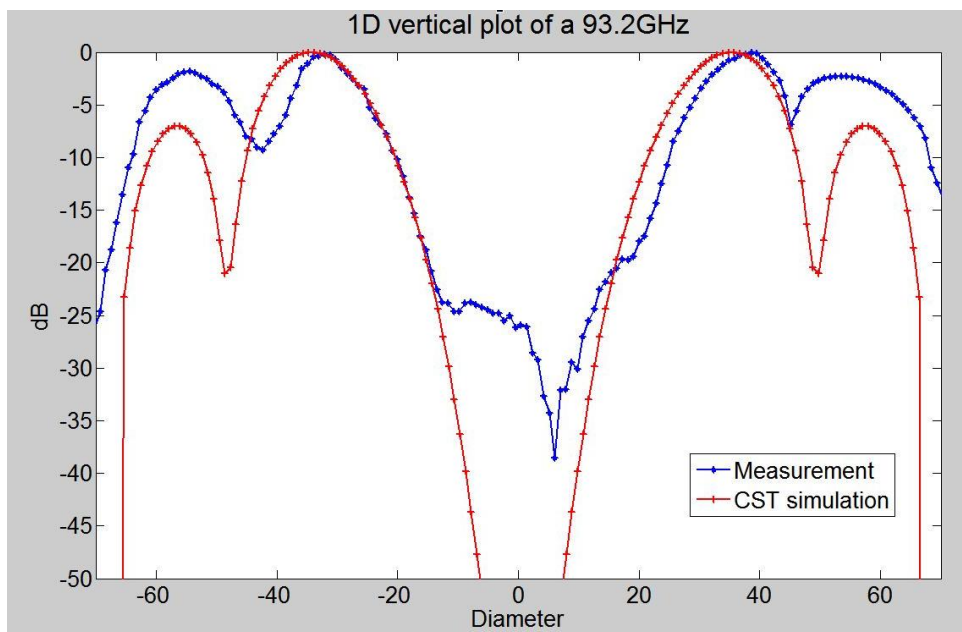


Figure 3-36: The most optimized 1D amplitude plot through rotating axis of measurement data.

The desired mode should occur at the aperture of a cavity. As shown in Figure 3-35, the exact mode did not occur. We got the most optimized 1D plot through rotating axis of measurement data in picture 3-36. We define a function called a 1D error function calculated by summing the difference results of the CST $E_{reference}(i)$ and measurement data $E_{measurement}(i)$ at every point as [45-47]

$$\text{error} = \frac{\sum_i (|E_{reference}(i)| - |E_{measurement}(i)|)^2}{\sum_i |E_{reference}(i)|^2} \quad (3.2)$$

The error function is shown in Fig. 3-36. An error coefficients are approximately 0.17796. The good matching coefficient indicates the amplitude intensity at aperture. However, one mirror system interferes with each beam propagation due to the narrow distance among the systems. In order to measure the desired mode patterns, we have designed two mirror systems.

3.3.4 Two mirror system of a mode generator

We measured one mirror system until now. However, due to the close proximity to arrange the each structures, one mirror system undergo interference such as coupling of the cavity, alignment, and unwanted interception form reflected beam.

The new mirror system will have the new t mirrors. The mirror design is started from beam waist of the corrugated feed horn. Fig. 3-37 shows the schematic of the beam of geometric optics. The mirror design is done using Gaussian optics. From Gaussian beam optics, Eq. (3.1) is useful.

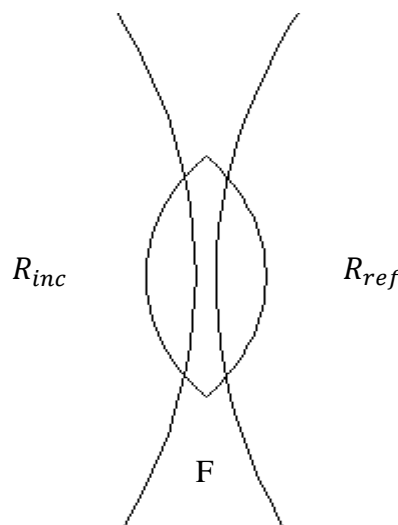


Figure 3-37: Curvature of a geometrical optics

As shown in Fig. 3-37, the mirror curvature can be determined by matching the incoming Gaussian beam with the reflecting Gaussian beam by means of the Eq. (3.3) [23].

$$\frac{1}{F} = \frac{1}{R_{inc}} + \frac{1}{R_{ref}} \quad (3.3)$$

The mirror curvature is then,

$$F = \frac{R_m}{2} \quad (3.4)$$

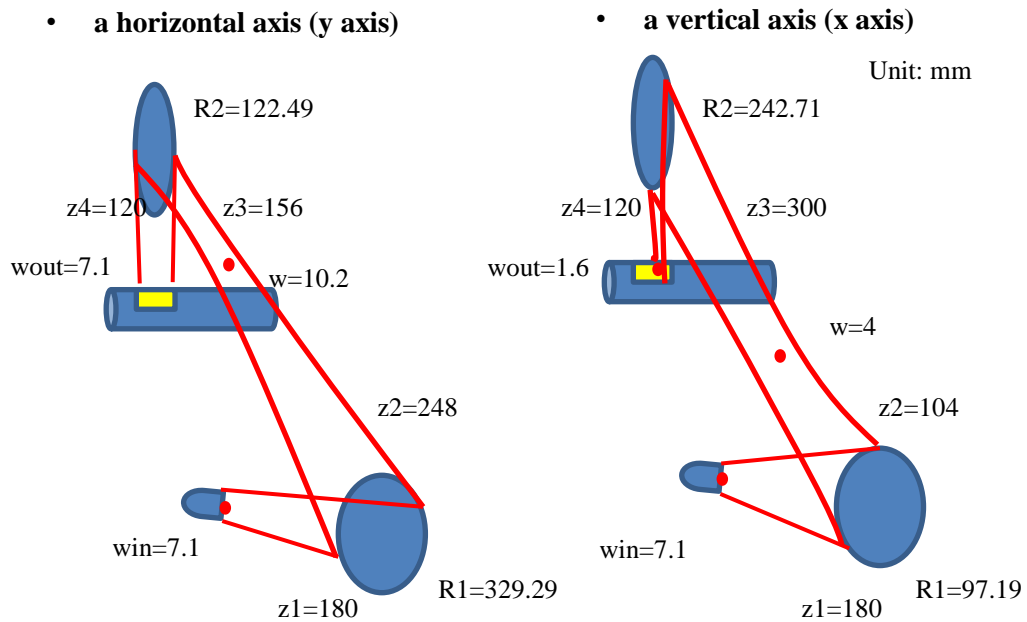


Figure3-38: Schematic of the two mirror system.

The measurement results of the mirror 1 are shown in Fig. 3-39 and 3-40. The red color represents the calculated beam sizes.

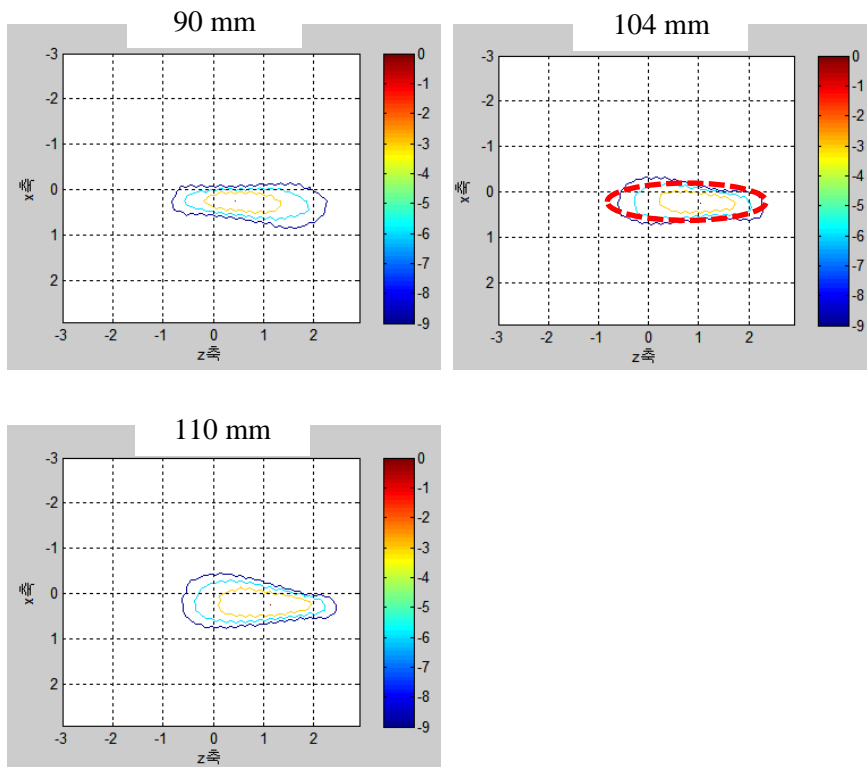


Figure 3-39: M1 measurement results for the vertical axis (by 12dB)

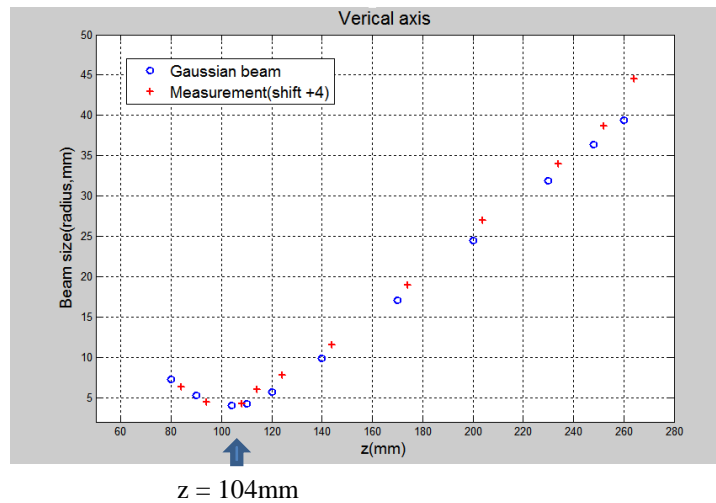


Figure 3-40: Comparison with ideally Gaussian beam and M1 measurement results for the vertical axis.

We didn't know the position of generating the beam waist in the corrugated feed horn. Therefore the beam waist could be a decisive factor in the mirror system. Based on this information, the measurement results could be +4 mm shift. As shown on Figure 3-40, the ideal beam size and the measured data can be seen almost similar.

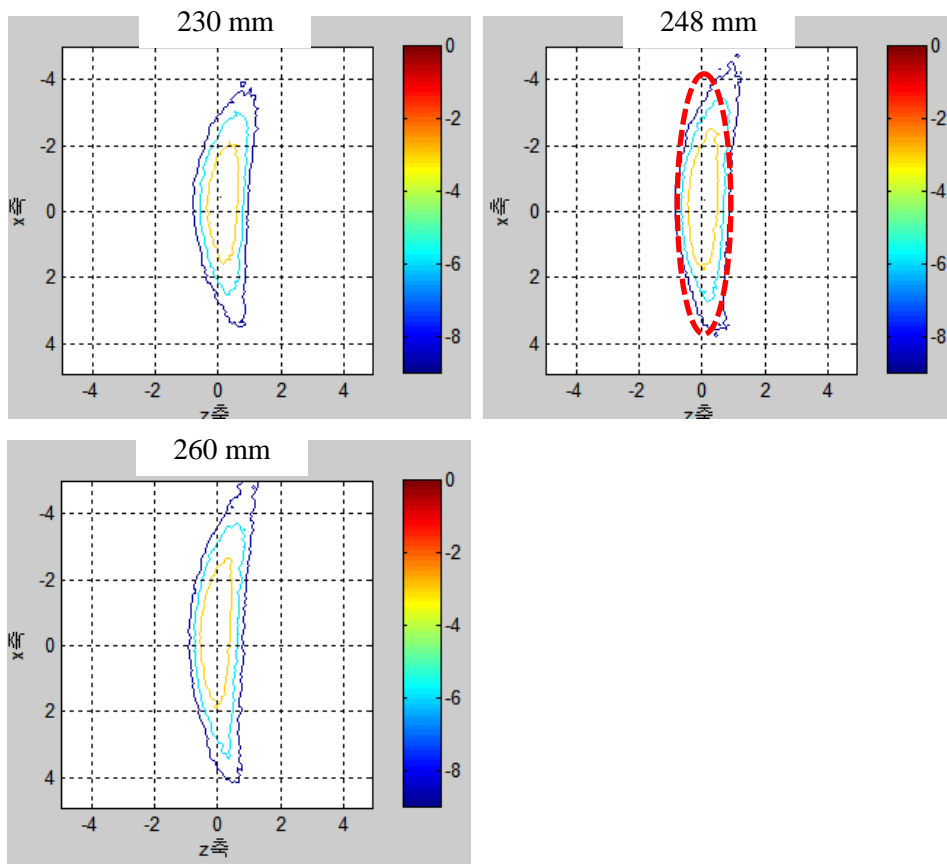


Figure 3-41: M1 measurement results for the horizontal axis.

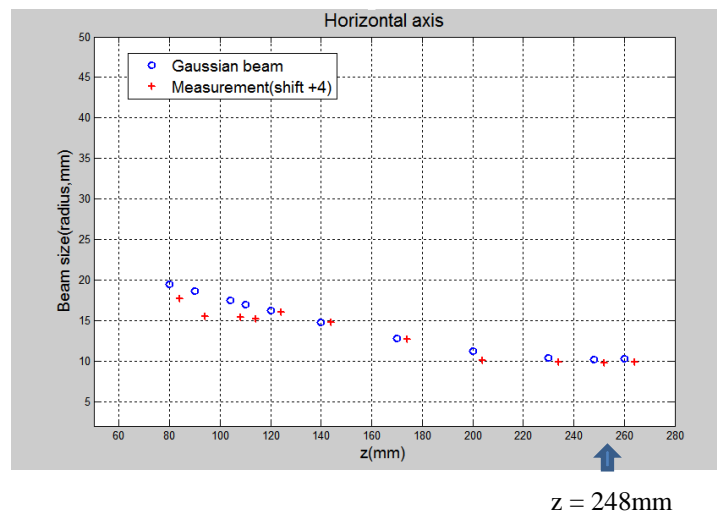


Figure 3-42: Comparison with ideally Gaussian beam and M1 measurement results for the horizontal axis.

The reflected beam from M2 is the smallest beam size, the beam size on 17.2×3.8mm is the last

beam size form M2.

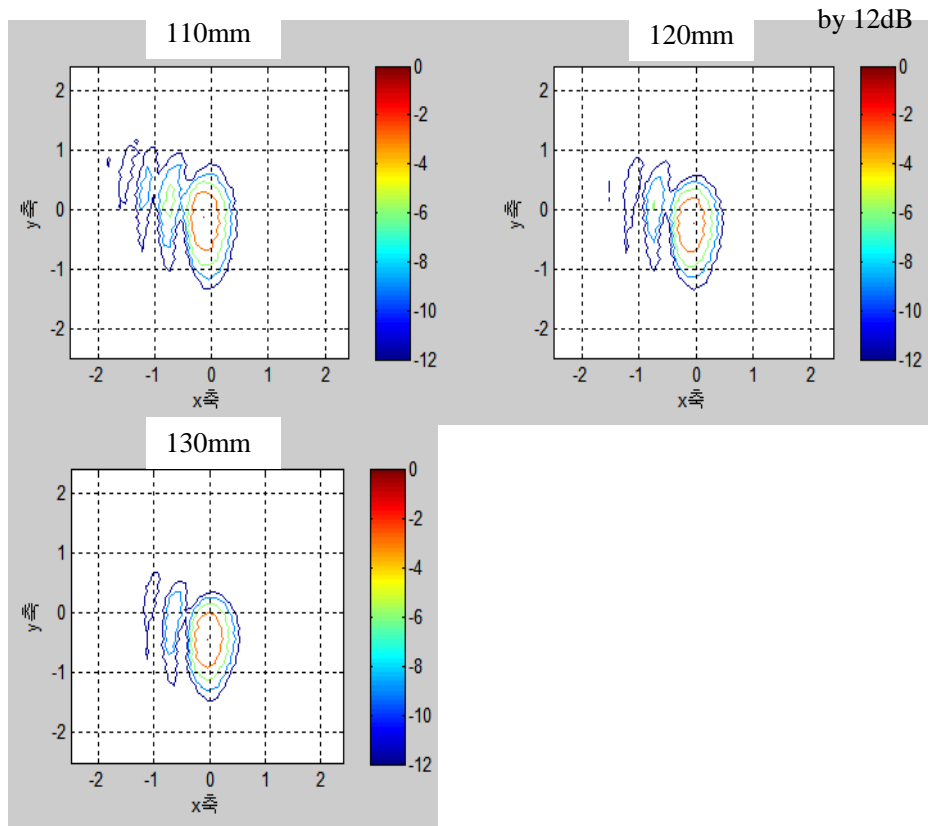


Figure 3-43: M2 measurement results (by 12dB)

Based on figure 3-43, we check the size of each axis of the beam. 120mm is located in the caustic of a cavity. The comparison with ideally Gaussian beam and M2 measurement results for the vertical axis is shown in Figure 3-44 and 3-45.

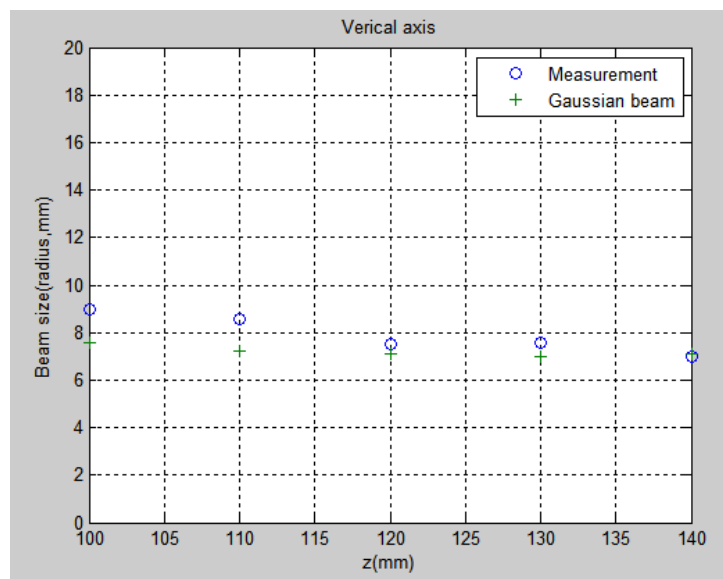


Figure 3-44: Comparison with ideally Gaussian beam and M2 measurement results for the vertical axis.

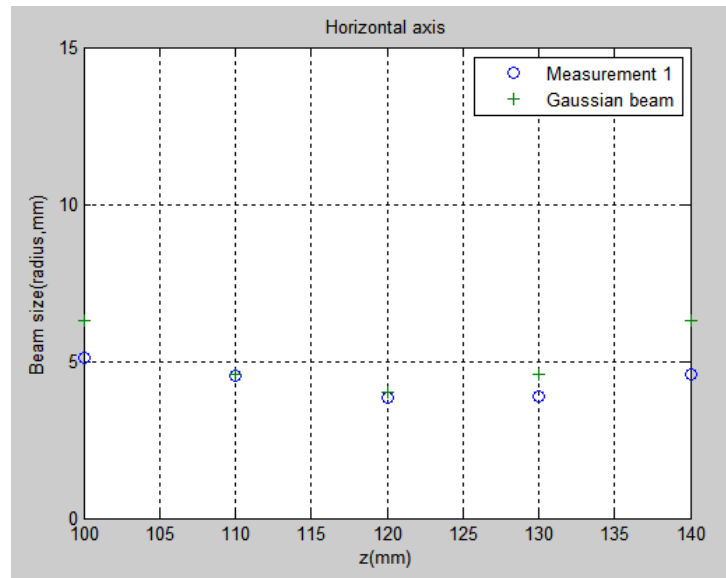


Figure 3-45: Comparison with ideally Gaussian beam and M2 measurement results for the horizontal axis.

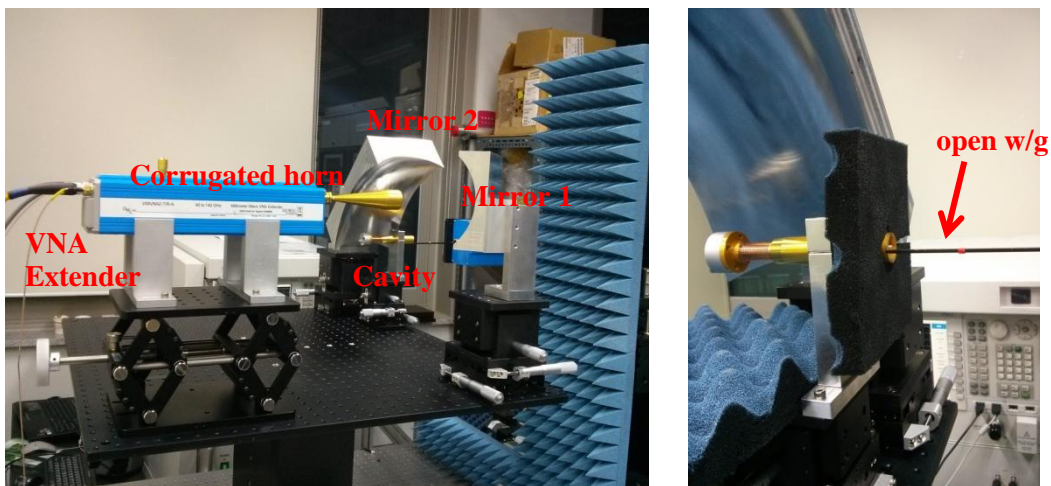


Figure 3-46: The measurement environment of two mirror system.

A measurement environment of two mirror system is shown in Fig. 3-46. When measuring the beam pattern, one has to consider many challenging parts such as alignment of mirrors. The measurement takes significant amount of time because the measurement is so sensitive to the alignment, position, and unwanted interceptions of the beams. The measurement results are the significant challenge, TE_{62} mode pattern will constantly try different ways.

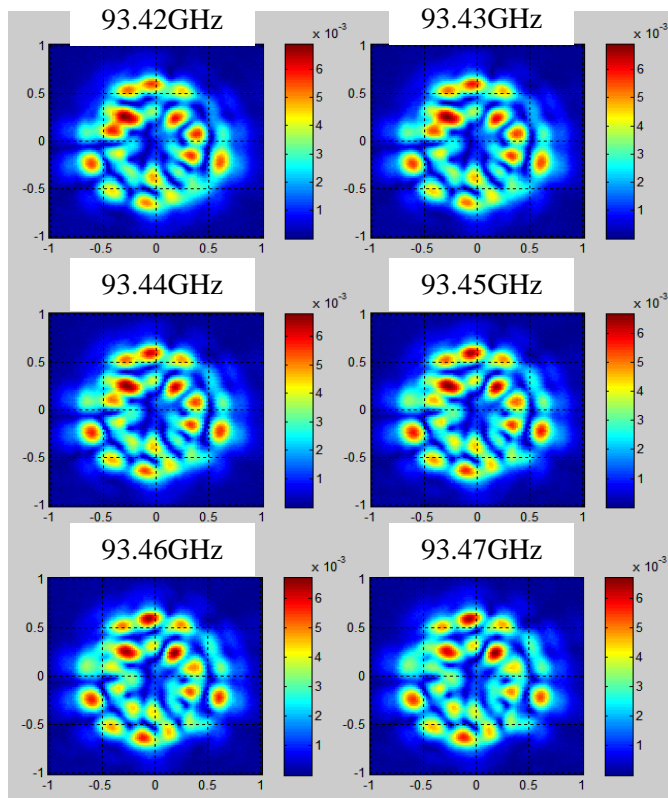


Figure 3-47: 1mm distance measurement from aperture to open waveguide probe, the vertical E-field magnitude pattern (Two mirror system).

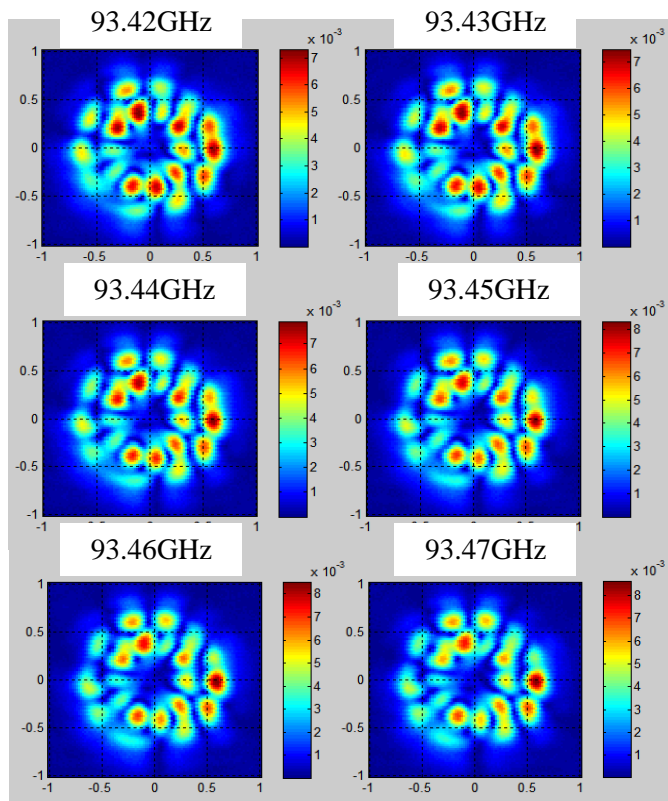


Figure 3-48: 1mm distance measurement from aperture to open waveguide probe, the horizontal E-field magnitude pattern (Two mirror system).

The pictures of the measurement results in each axis are shown in Fig.3-47 and 3-48. We should check mode pattern of sum plot in each axis. After that, measurement data are compared with reference data that show 1D plot of radial and azimuthal axis.

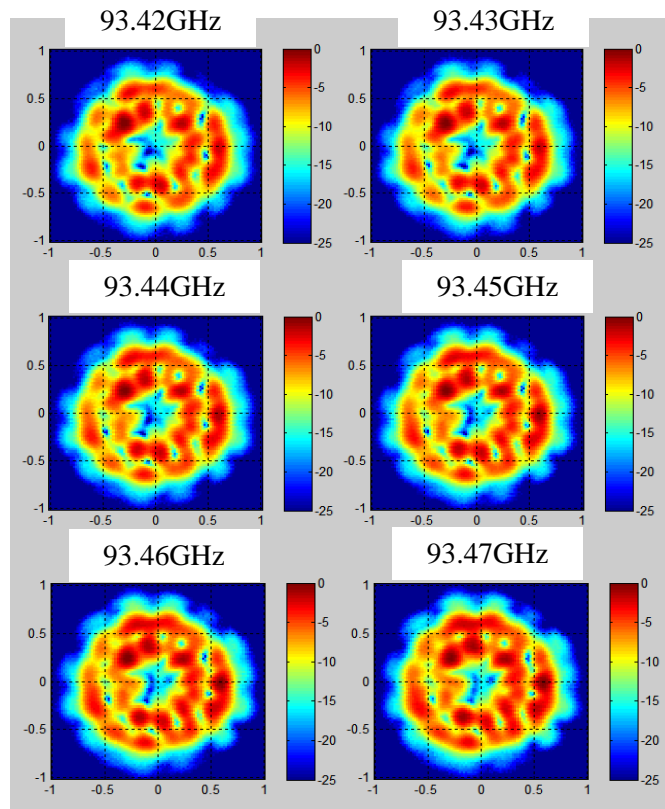


Figure 3-49: 1mm distance measurement from aperture to open waveguide probe. The dB sum of vertical and horizontal axis (Two mirror system).

The sum result of polarizations is shown in Fig. 3-49. TE₆₂-like mode on hole structure cavity is found in W band between 93 and 94GHz. We can be found that TE₆₂ mode at radial axis showed at aperture, it should be analyzed optimization for 1D plot. However, mode pattern at radial axis can not see. So the distance of measured the beam pattern was changed to 10mm.

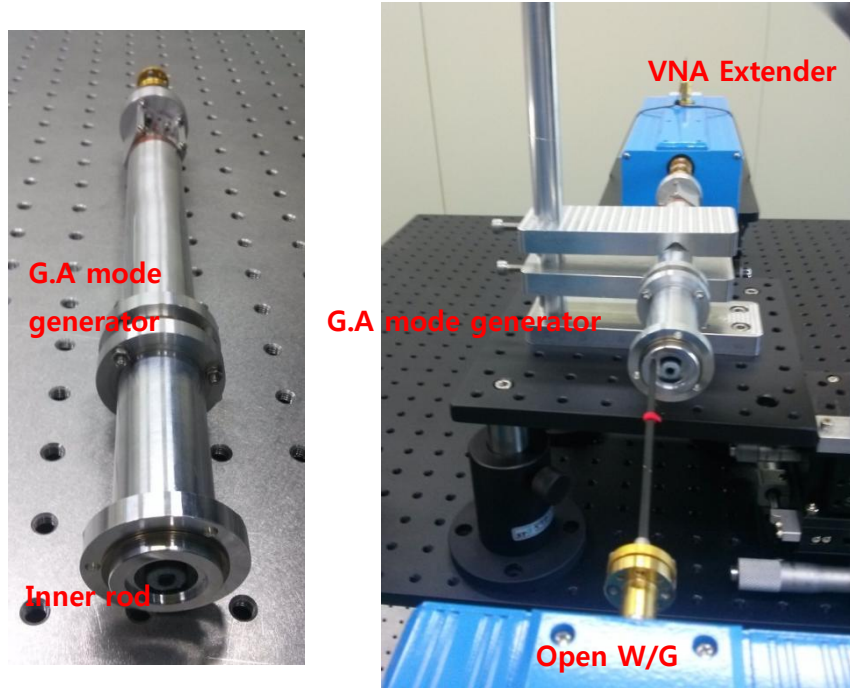


Figure 3-50: The measurement environment of G.A mode generator.

At figure3-50, TE mode generator was manufactured by General Atomics in the USA. it was compared with our designed mode generator. To check the TE_{62} mode as shown in Figure 3-50, GA mode generator was set as reference. Based on the measurement results of General Atomics generator, we were compared with rotating mode pattern in the cavity.

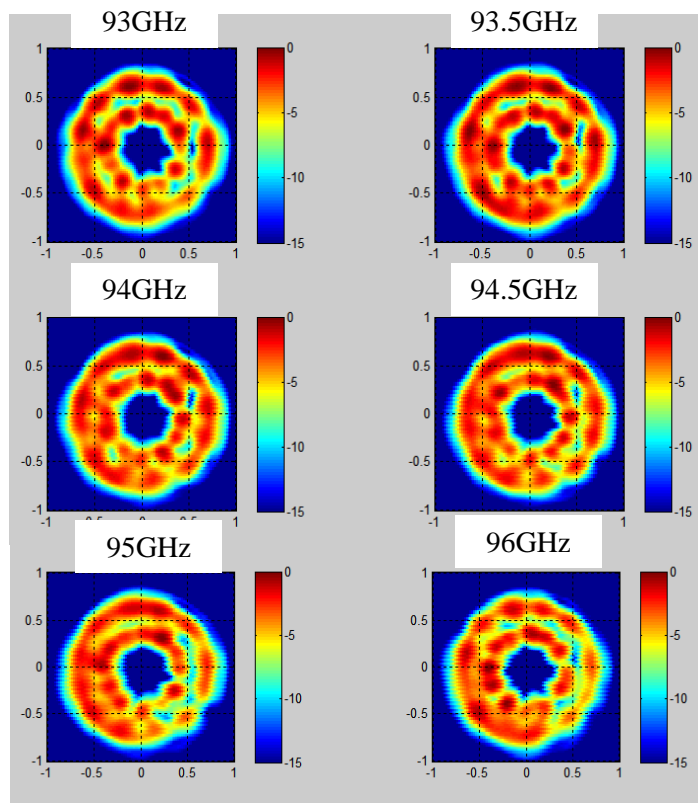


Figure 3-51: 1mm distance measurement from aperture of G.A generator to open waveguide probe.
The dB sum of vertical and horizontal axis.

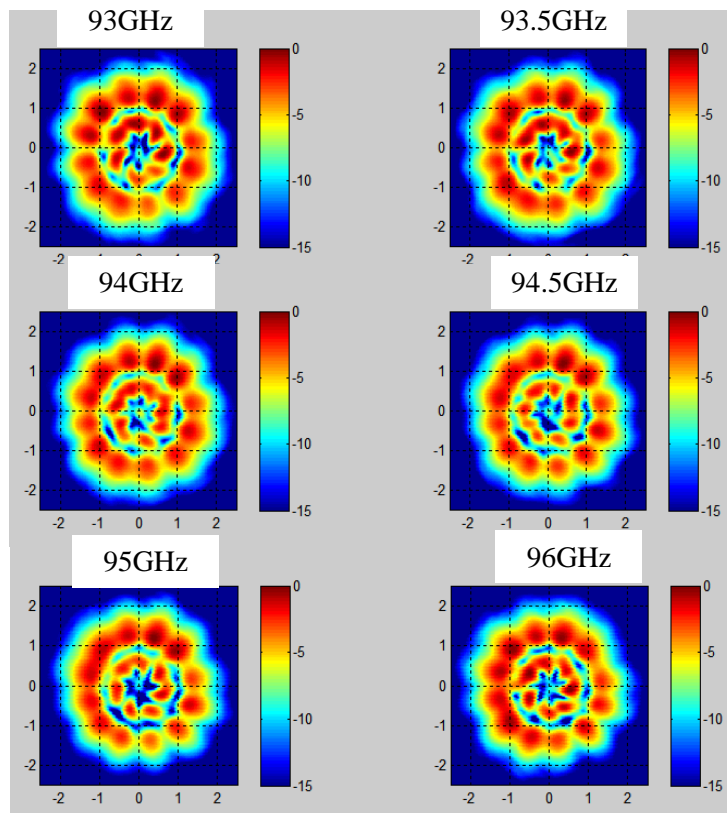


Figure 3-52: 10mm distance measurement from aperture of G.A generator to open waveguide probe. The dB sum of vertical and horizontal axis.

The measurement result of G.A generator is shown in Figure 3-51. It is E-field pattern of 1mm distance from aperture to open waveguide. TE_{62} mode pattern was also checked at radial axis. the intensity in the center part of cavity can be see the lowest power and other modes do not occur.

Figure3-52 is measurement results by changing the distance from aperture to waveguide as 10mm. We confirmed TE mode pattern at radial axis as figure 3-51. we should check 1D in order to confirm radial plot.

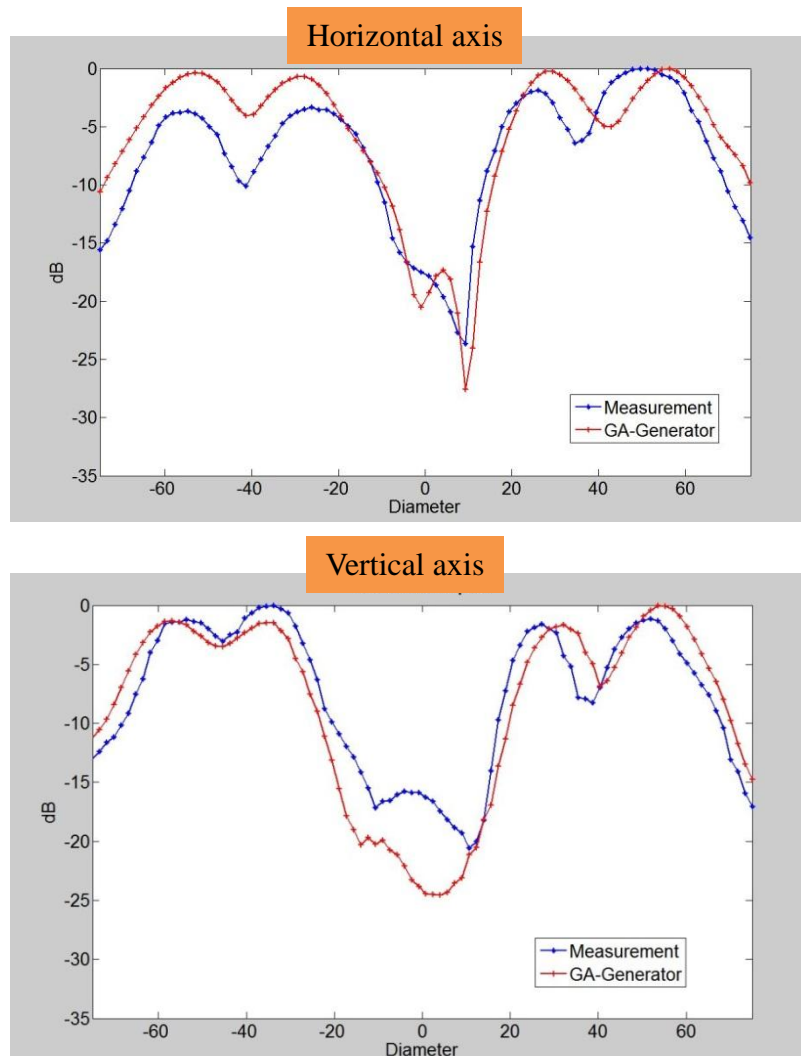


Figure 3-53: The most optimized 1D amplitude at radial axis plot through rotating axis of measurement data. Measurement result of UNIST mode generator was compared with G.A generator data.

As figure 3-53, hole structure generator (UNIST mode generator) is compared with G.A generator about 1D plot at radial axis. the errors are either 0.09606 or 0.099543 in perpendicular and parallel direction.

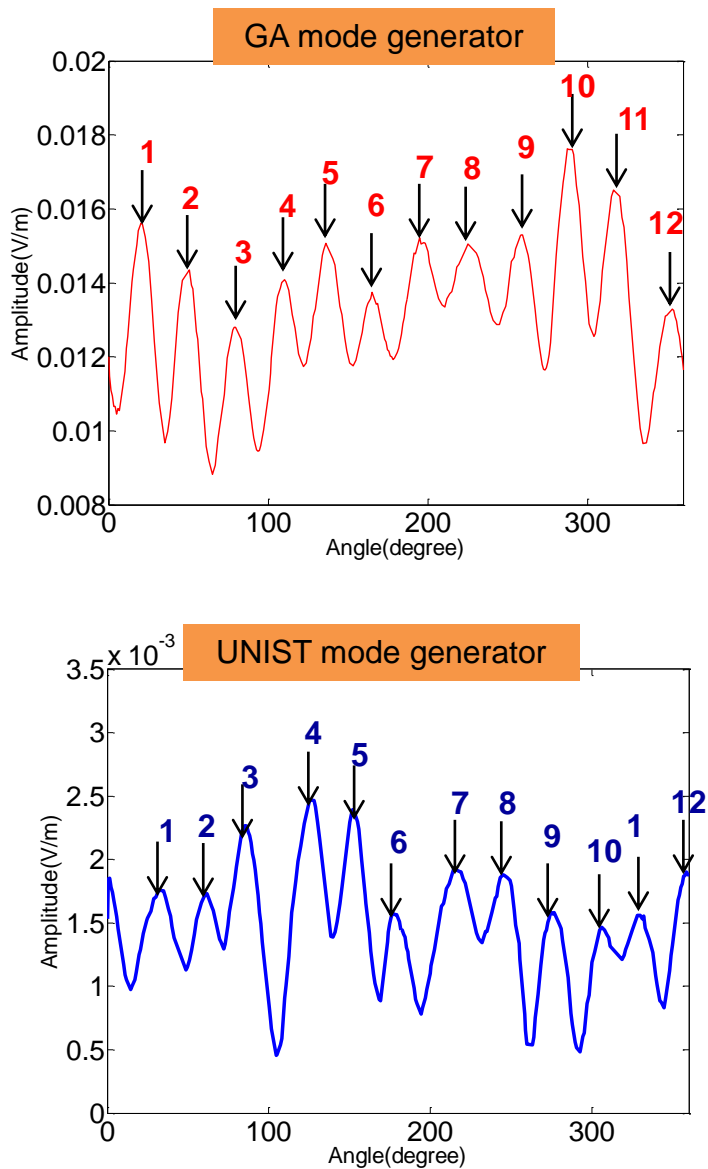


Figure 3-54: The most optimized 2D amplitude at azimuthal axis plot through rotating axis of measurement data. Measurement result of UNIST mode generator was compared with G.A generator data.

The peaks at azimuthal axis were shown both G.A generator and UNIST mode generator in figure 3-52. These are consistent with the number of peaks with TE_{6n} mode. When you see figure 3-51 and 3-52, the optimized 1d plot was coincide with te_{62} mode.

chapter 4

Summary & conclusion

In this thesis, I proposed experimental study on generation of a higher order mode for W-band gyrotron oscillator. The purpose for this study was to generate the desired mode at aperture of a cavity. The quasi-optical system was designed to convert the input Gaussian-like beam to a beam pattern which will excite the TE_{62} mode at the aperture of a cavity. The design of a mode generator has been carried out using Ansoft HFSS and CST software and validated with experimental results.

This way of mode excitation is especially useful for the cold test. The results of Mirrors between the analytic solutions and the simulations match remarkably well. However, the cavity part seems to need more research. The measurement is very sensitive on the experimental condition such as alignment, coupling of the cavity, and unwanted interception from reflected beam.

This mode generator is successfully designed to perform low power verification of the quasi optical system for a W-band TE_{62} mode. The electric field pattern at output of the cavity is under investigation about back propagation.

REFERENCES

1. N.L. Alexandrov, G.G. Denisov, D.R Whaley & M.Q. Tran, "Low power excitation of gyrotron-type modes in cylindrical modes in cylindrical waveguide using quasi-optical technique" Submitted for publication to Int. F. of Electronics, Vol. 79, Issue 2, p. 215-226, 1995
2. D. Wagner, M. Thumm and A. Arnold, "Mode generator for the cold test of step-tunable gyrotrons", IEEE, p. 303-304, Sept. 2002
3. Andreas Arnold, Oliver Prinz, Dietmar Wagner and Manfred Thumm, "Operation of a Quasioptical Multi-Mode Generator for 105-150GHz", IRMMW-THz, p. 434-435, Sept. 2007
4. K. H. Kim, E. M. Choi, 2012, "Design Study of a 95GHz, TE_{62} mode generator", Contents Copyright 2012 The Institute of Electronics Engineers of Korea, Vol. 35, P 52
5. T.S. Chu, M. Blank, S. Cauffman, K. Felch, H. Jory, "Design and Demenstration of a $TE_{22.6}$ Mode Generator for Testing Internal Converter of a Gyrotron", IEEE, p. 26. Sept. 2006
6. Greg Gbur, Emil Wolf, "The Ryleigh Range of Partically Coherent Beams", Optics Communications, Volume 199, Issues 5-6, p. 295-304, 2001
7. William H. Carter, "Electromagnetic Field of a Gaussian Beam with an Elliptical Cross Section", Journal of the optical society of America, Vol. 62, Number 10. P. 1195-1201, 1972
8. D. Wagner, M. Blank, T. S. Chu, K. Felch, M. Mizuhara, "Mode generators for high order rotating gyrotron modes", Infrared and Millimeter Waves, p. 271-272, Sept. 2000,
9. Washington, D. C, "High-Magnetic-Field Research and Facilities", National Academy of Sciences, p. 51
10. James P. Anderson, "Experimental Study of a 1.5 MW, 110 GHz Gyrotron Oscillator", PhD thesis, Massachusetts Institute of Technology, Elec. Engrg. And Comp. Sci. Eept., 2005
11. D. Wagner, M. Thumm, G. Gantenbein, W.Kasperek, and T. Idehara, "Anylsis of a complete gyrotron oscillator using the scattering matrix description", International Journal of Infrared and Millimeter Waves, Vol. 19, No. 2, p. 185-194, 1997
12. L. D. Dickson, "Characteristics of a Propagating Gaussian Beam", Applied Optics, Vol. 9, Issue 8, pp. 1854-1861, 1970

13. Saleh, Bahaa E. A and Teich, Malvin Carl, "Fundamentals of Photonics", John Wiley & Sons. Chapter3, p. 80-107, http://en.wikipedia.org/wiki/Gaussian_beam
14. Cvimellesgriot.com, "Gaussian Beam Optics", <https://www.cvimellesgriot.com/Products/Documents/TechnicalGuide/Gaussian-Beam-Optics.pdf>
15. Oleg V. Ivanov, "Propagation and coupling of hybrid modes in twisted fibers", JOSA A, Vol. 22, No. 4, pp. 716-723, 2005
16. Carlos del Río Bocio, "Modern Corrugated Horn Antenna," Ph.D dissertation, Departamento de Ingeniería Eléctrica y Electrónica, Universidad Pública de Navarra, Pamplona, 2003
17. C. del Rio, J. Teniente, R. Gonzalo and M. Sorolla, " On The determination of The Phase Center of Gaussian Horn Antenns", Electronic Engineering Department Universidad Publica de Navarra campus Arrosadia, 1998
18. Richard J. Wylde and Derek H. Martin, "Gaussian Beam-Mode Analysis and Phase-Centers of Corrugated Feed Horns", IEEE transactions on microwave theory and techniques, Vol. 41, No. 10. P. 1691-1699, Oct. 1993
19. Jorge Teniente Vallinas, Dr. Carlos del Río Bocio, Grupo de Antenas, "Modern Corrugated Horn Antennas," Departamento de Ingeniería Eléctrica Electrónica Universidad Pública de Navarra, Pamplona, 2003
20. Ramon Gonzalo, Jorge Teniente and Carlos del Rio, "Gaussian profiled horn antennas", On The Determination of The Phase Center of Gaussian, 1996
21. M. A. Lieb and A. J. Meixner, "A high number aperture parabolic mirror as imaging device for confocal microscopy", The international online journal of optics, Vol. 8, Iss. 7, pp 458-474, 2001
22. KwangHoon Kim, MunSeok Choe, WooSang Lee, JoonHo So, EunMi Choi, "Generation of Higher order Mode for W-ban Gyrotron Oscillator", Neo-technology Energy Weapons Conference, p. 22-25, 2012
23. PAUL F. GOLDSMITH, "Quasioptical Systems", ISBN 0-7803-3439-6, p106-111
24. David M. Pozar, "Microwave Engineering", Second Edition, ISBN 0-471-17096-8, p 6-7
25. Antonio C. Torrezan de Sousa, "Frequency-Tunable Second-Harmonic Submillimeter-Wave

- Gyrotron Oscillators”, in partial fulfillment of the requirements for the degree of Doctor of Philosophy at the MIT, 99-105, 2010
26. M. A. Shapiro, R. J. Temkin, “Calculation of a Hyperbolic Corrugated Horn Converting the TEM₀₀ Mode to the HE₁₁ Mode,” *Journ. Infrared Milli Terahz Waves*, Vol. 32, No. 3, pp. 283-294, 2011
 27. Carlos del R o Bocio, "Modern Corrugated Horn Antenna," Ph.D dissertation, Departamento de Ingenier a El ctrica y Electr nica, Universidad P blica de Navarra, Pamplona, 2003
 28. M. Thumm, V. Erckmann, W. Kasperek, H. Kumric, G. A. Muller, P. G. Schuller and R. Wilhelm, “Very high power mm-wave components in oversized waveguides,” *Microwave Journal*, pp. 103-121, 1986
 29. J. L. Doane, “Low loss propagation in corrugated rectangular waveguide at 1mm wavelength,” *Int. Jour. Infrared Millimeter Waves*, vol. 8, no. 1, pp.13-27, 1987
 30. G. L. James and B. M. Thomas, “TE₁₁ to HE₁₁ cylindrical waveguide mode converters using ring-loaded slots,” *IEEE Trans. Microwave Theory and Tech.*, vol. 30, no. 3, pp. 278-285, 1982
 31. M. Thumm, V. Erckmann, W. Kasperek, H. Kumric, G. A. Muller, P. G. Schuller and R. Wilhelm, “Very high power mm-wave components in oversized waveguides,” *Microwave Journal*, pp. 103-121, 1986
 32. J. L. Doane, “Compact HE₁₁ to surface wave converters for high power waveguide dummy loads,” *Int. Jour. Infrared and Millimeter Waves*, vol. 14, no. 2, pp. 363-382, 1993
 33. H. S. Lee and H. J. Eom, “Radiation from a corrugated circular waveguide with a flange,” *Jour. of Electromagnetic Waves and Appl.*, vol. 16, no. 9, pp. 1255-1274, 2002
 34. J. Teniente, R. Gonzalo, C. Rio, J. Marti-Canales, M. Sorolla, A. Fernandez, K. M. Likin, and R. Martin, “Corrugated horn antenna for low-power testing of the quasioptical transmission lines at TJ-II stellerator,” *Int. Jour. Infrared and Millimeter Waves*, vol. 20, no. 10, pp. 1757-1767, 1999
 35. L. C. D. Silva, “A method of analysis of TE₁₁ to HE₁₁ mode converters,” *IEEE Trans. Microwave Theory and Tech.*, vol. 36, no. 3, 1988
 36. P. J. B. Clarricoats and A. D. Olver, “Corrugated horns for microwave antennas”, *IEE Electromagnetic Waves Series 18*, Peter Peregrinus Ltd., 1984.

37. BRUCE MACA. THOMAS, SENIOR MEMBER, "Design of Corrugated Conical Horns", IEEE, Vol. AP-26, No. 2, March 1978
38. Richard J. Wylde and Derek H. Martin, "Gaussian Beam-Mode Analysis and Phase-Centers of Corrugated Feed Horns", IEEE transaction on microwave theory and techniques, Vol. 10, No. 10, 1691-1699, 1993
39. Xiaolei Zhang, "Design of Conical Corrugated Feed Horns for Wide-Band High-Frequency Applications", IEEE transaction on microwave theory and techniques, Vol. 41, No. 8, 1263-1274, 1993
40. Taeho Son, Seog-Tae Han and Byungsoo Lee, "85 - 115GHz Corrugated Conical Horn Antenna for the Radio Telescope System", IEEE, Volume 2, 324-327, 2001
41. Paul F. Goldsmith, "Quasi-Optical Techniques", PROCEEDINGS OF THE IEEE, VOL. 80, NO. 11, 1729-1747, 1992
42. P. J. Castro, J. J. Barroso, and R. A. Correa, "Cold Tests of Open Coaxial Resonators in the Range 9-17GHz", International Journal of Infrared and Millimeter Waves, Vol. 14, No. 2, Issue 2, pp 383-395, 1993
43. J. Neilson, "Surf3d and Tol: Computer codes for design and analysis of high-performance QO Launchers in Gyrotrons", IEEE, 667-668, 2004
44. R. D. Elliot and P. J. B. Clarricoats, "Corrugated waveguide monopulse feed," Electron. Lett., vol. 16, no. 9, pp. 324-325, 1980
45. Hiroshi Idei, Takashi Shimozuma, Michael A. Shapiro, Takashi Notake, Shin Kubo, and Richard J. Temkin, "Experimental Verification of Phase Retrieval of Quasi-optical Millimeter-Wave Beams", IEEE Transactions on microwave theory and techniques, Vol. 54, No. 11, pp. 3899-3905, 2006
46. Sudheer Jawla, Jean-Philippe Hogge, and Stefano Alberti, "Theoretical Investigation of Iterative Phase Retrieval Algorithm for Quasi-Optical Millimeter-Wave RF Beams", IEEE transactions on plasma science, Vol. 37, No. 3, pp. 403-413, 2009
47. N. L. Aleksandrov, A. V. Chirkov, G. G. Denisov, and S. V. Kuzikov, "Mode Content Analysis from Intensity Measurements in A few Cross Sections of Oversized Waveguides", International Journal of Infrared and Millimeter Waves, Vol. 18, No. 8, pp. 1505-1516, 1997